

The clustering of galaxies in the completed SDSS-III Baryon Oscillation Spectroscopic Survey: tomographic BAO analysis of DR12 combined sample in Fourier space

Gong-Bo Zhao^{1,2*}, Yuting Wang^{1,2}, Shun Saito^{3,4}, Dandan Wang¹, Ashley J. Ross^{5,2}, Florian Beutler^{2,6}, Jan Niklas Grieb^{7,8}, Chia-Hsun Chuang^{9,10}, Francisco-Shu Kitaura¹⁰, Sergio Rodriguez-Torres^{9,11,12}, Will J. Percival², Joel R. Brownstein¹³, Antonio J. Cuesta¹⁴, Daniel J. Eisenstein¹⁵, Héctor Gil-Marín^{16,17,2}, Jean-Paul Kneib¹⁸, Robert C. Nichol², Matthew D. Olmstead¹⁹, Francisco Prada⁹, Graziano Rossi²⁰, Salvador Salazar-Albornoz^{21,22}, Lado Samushia², Ariel G. Sánchez²², Daniel Thomas², Jeremy L. Tinker²³, Rita Tojeiro²⁴, David H. Weinberg^{25,5}, Fangzhou Zhu²⁶

¹ National Astronomy Observatories, Chinese Academy of Science, Beijing, 100012, P.R.China

² Institute of Cosmology & Gravitation, University of Portsmouth, Dennis Sciama Building, Portsmouth, PO1 3FX, UK

³ Max-Planck-Institut für Astrophysik, Karl-Schwarzschild-Strasse 1, D-85740 Garching bei München, Germany

⁴ Kavli Institute for the Physics and Mathematics of the Universe (IPMU), The University of Tokyo, Kashiwa, Chiba 277-8583, Japan

⁵ Center for Cosmology and AstroParticle Physics, The Ohio State University, Columbus, OH 43210, USA

⁶ Lawrence Berkeley National Lab, 1 Cyclotron Rd, Berkeley CA 94720, USA

⁷ Max-Planck-Institut für extraterrestrische Physik, Postfach 1312, Giessenbachstr, 85741 Garching, Germany

⁸ Universitäts-Sternwarte München, Ludwig-Maximilians-Universität München, Scheinerstraße 1, 81679 München, Germany

⁹ Instituto de Física Teórica, (UAM/CSIC), Universidad Autónoma de Madrid, Cantoblanco, E-28049 Madrid, Spain

¹⁰ Leibniz-Institut für Astrophysik Potsdam (AIP), An der Sternwarte 16, 14482 Potsdam, Germany

¹¹ Campus of International Excellence UAM+CSIC, Cantoblanco, E-28049 Madrid, Spain

¹² Departamento de Física Teórica, Universidad Autónoma de Madrid, Cantoblanco, E-28049 Madrid, Spain

¹³ Department of Physics and Astronomy, University of Utah, 115 S 1400 E, Salt Lake City, UT 84112, USA

¹⁴ Institut de Ciències del Cosmos (ICCUB), Universitat de Barcelona (IEEC- UB), Martí i Franquès 1, E-08028 Barcelona, Spain

¹⁵ Harvard-Smithsonian Center for Astrophysics, 60 Garden St., Cambridge, MA 02138, USA

¹⁶ Sorbonne Universités, Institut Lagrange de Paris (ILP), 98 bis Boulevard Arago, 75014 Paris, France

¹⁷ Laboratoire de Physique Nucléaire et de Hautes Energies, Université Pierre et Marie Curie, 4 Place Jussieu, 75005 Paris, France

¹⁸ Laboratoire d’Astrophysique, Ecole Polytechnique Fédérale de Lausanne (EPFL), Observatoire de Sauverny, CH-1290 Versoix, Switzerland

¹⁹ Department of Chemistry and Physics, King’s College, 133 North River St, Wilkes Barre, PA 18711, USA

²⁰ Department of Astronomy and Space Science, Sejong University, Seoul 143-747, Korea

²¹ Universitäts-Sternwarte München, Ludwig-Maximilians-Universität München, Scheinerstraße 1, 81679 München, Germany

²² Max-Planck-Institut für extraterrestrische Physik, Postfach 1312, Giessenbachstr, 85741 Garching, Germany

²³ Center for Cosmology and Particle Physics, Department of Physics, New York University, 4 Washington Place, New York, NY 10003, USA

²⁴ School of Physics and Astronomy, University of St Andrews, North Haugh, St Andrews KY16 9SS, UK

²⁵ Department of Astronomy, The Ohio State University, 140 West 18th Avenue, Columbus, OH 43210, USA

²⁶ Department of Physics, Yale University, New Haven, CT 06511, USA

ABSTRACT

We perform a tomographic baryon acoustic oscillations (BAO) analysis using the monopole, quadrupole and hexadecapole of the redshift-space galaxy power spectrum measured from the pre-reconstructed combined galaxy sample of the completed Sloan Digital Sky Survey (SDSS-III) Baryon Oscillation Spectroscopic Survey (BOSS) Data Release (DR)12 covering the redshift range of $0.20 < z < 0.75$. By allowing for overlap between neighbouring redshift slices, we successfully obtained the isotropic and anisotropic BAO distance measurements within nine redshift slices to a precision of $1.5\% - 3.4\%$ for D_V/r_d , $1.8\% - 4.2\%$ for D_A/r_d and $3.7\% - 7.5\%$ for $H r_d$, depending on effective redshifts. We provide our BAO measurement of D_A/r_d and $H r_d$ with the full covariance matrix, which can be used for cosmological implications. Our measurements are consistent with those presented in Alam et al. (2016), in which the BAO distances are measured at three effective redshifts. We constrain dark energy parameters using our measurements, and find an improvement of the Figure-of-Merit of dark energy in general due to the temporal BAO information resolved. This paper is part of a set that analyses the final galaxy clustering dataset from BOSS.

Key words:

Baryon acoustic oscillations; Dark energy; Galaxy survey

1 INTRODUCTION

One of key science drivers of large spectroscopic galaxy surveys is to unveil the nature of dark energy (DE), the unknown energy component with a negative pressure to drive the accelerating expansion of the Universe (Riess et al. 1998; Perlmutter et al. 1999). The equation-of-state (EoS) function $w(z)$, which is the ratio of pressure over energy density of DE and is a function of redshift z in general, is a proxy linking the nature of DE and its phenomenological features which can be probed by observations. For instance, a observational confirmation of $w = -1$ may suggest that DE is essentially vacuum energy, while a time-evolving w can be a sign of new physics, *e.g.*, dynamical dark energy scenarios (Peebles & Ratra 1988; Ratra & Peebles 1988; Caldwell 2002; Feng et al. 2005; Armendariz-Picon et al. 2000), or a breakdown of general relativity on cosmological scales (see Clifton et al. 2012 for a recent review of modified gravity theories). Therefore reconstructing $w(z)$ directly from data is an efficient way for DE studies (Weinberg et al. 2013; Zhao et al. 2012; Sahni & Starobinsky 2006).

The function $w(z)$ of DE leaves imprints on the cosmic background expansion history, which can be probed by the effect of baryon acoustic oscillations (BAO) measured from galaxies surveys (Eisenstein et al. 2005; Cole et al. 2005), besides other probes including supernovae Type Ia (SN Ia) (Riess et al. 1998; Perlmutter et al. 1999), cosmic microwave background (CMB) (Planck Collaboration et al. 2015) and so forth. BAO is a characteristic three-dimensional clustering pattern of galaxies at about 150 Mpc on the comoving scale, due to sound waves generated by the photon-baryon coupling in the early universe (Peebles & Yu 1970; Sunyaev & Zeldovich 1970; Eisenstein & Hu 1998). The BAO distance is traditionally measured using two-point correlation functions or power spectrum of galaxies. Recent studies find that higher-order statistics of galaxies (Slepian et al. 2016), or two-point clustering of voids can also be used for BAO measurements (Kitaura et al. 2016a)¹. Since the BAO scale is sensitive to cosmic geometry and it

is largely immune to systematics (Ross et al. 2011), BAO is widely used as the ‘standard ruler’ to calibrate the Universe.

Under assumptions that the BAO scale is the same in all directions with respect to the line-of-sight (l.o.s.) of the observer, one can probe the isotropic, one-dimensional (1D) BAO signal $D_V(z) \equiv [cz(1+z)^2 D_A(z)^2 H^{-1}(z)]^{1/3}$, where $D_A(z)$ and $H(z)$ are the angular diameter distance and Hubble parameter at an effective redshift z of the galaxy sample, using the monopole of the correlation function of power spectrum of galaxies in redshift space.

In fact, $D_A(z)$ and $H(z)$ can be separately measured when higher-order multipoles, *e.g.*, the quadrupole and hexadecapole, are included in the analysis. This is due to the Alcock-Paczynski (AP) effect (Alcock & Paczynski 1979): if one uses a wrong cosmology to convert redshifts into distances for the clustering analysis, the scales along and cross the l.o.s. will be dilated differently, which produces a measurable effect to break the degeneracy between D_A and H in the anisotropic, two-dimensional (2D) BAO analysis. The 2D BAO distances are more challenging to measure, but it is much more informative for DE studies because $w(z)$ is closely related to the first derivative of $H(z)$, but to the second derivative of $D_V(z)$.

The 1D and 2D BAO signals have been detected by a number of large galaxy surveys including the Sloan Digital Sky Survey (SDSS) (Eisenstein et al. 2005; Percival et al. 2010; Anderson et al. 2012, 2014a; Gil-Marín et al. 2015; Cuesta et al. 2016; Alam et al. 2016; Beutler et al. 2016a,b; Ross et al. 2016), the 2-degree Field Galaxy Redshift Survey (2dFGRS) (Cole et al. 2005), WiggleZ (Blake et al. 2011; Parkinson et al. 2012), the 6-degree Field Galaxy Survey (6dFGS) (Beutler et al. 2011) and so on. The Baryon Oscillation Spectroscopic Survey (BOSS) (Anderson et al. 2014b), part of SDSS III project (Eisenstein et al. 2011), has reached percent level BAO measurements at $z_{\text{eff}} = 0.32$ and $z_{\text{eff}} = 0.57$ (Anderson et al. 2014a; Gil-Marín et al. 2015; Cuesta et al. 2016; Beutler et al. 2016a; Ross et al. 2016) using the ‘low-redshift’ (LOWZ; $0.15 < z < 0.43$) and ‘constant stellar mass’ samples (CMASS; $0.43 < z < 0.7$) of Data Release (DR) 12 (Alam et al. 2015)².

¹ Email: gbzhao@nao.cas.cn

¹ In this work, we focus on galaxies as cosmic tracers thus will only refer to galaxies when discussing BAO measurements.

² The DR12 dataset is publicly available at <http://www.sdss.org/dr12/>

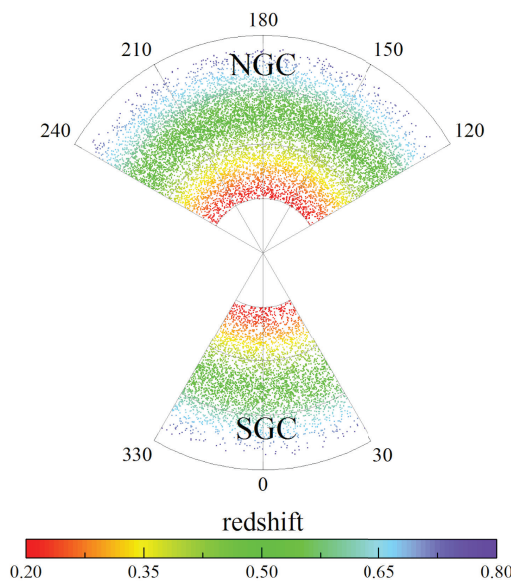


Figure 1. A wedge plot of the DR12 galaxies in the redshift range of $0.2 < z < 0.75$ in the NGC (upper part) and the SGC (lower part).

It is true that using galaxies across wide redshift ranges can yield a precise BAO measurement at a single effective redshift, but this does not capture the tomographic information in redshift, which is required for the study of $w(z)$. Subdividing the galaxy sample into a small number of independent redshift slices and perform the BAO analysis in each slice can in principle recover the temporal information to some extent (see Chuang et al. 2016 for a 4-bin BAO analysis of the BOSS DR12 sample). However, as the slice number increases, galaxies in each slice decrease, and we are at a risk of ending up with a seriously biased measurement due to large systematic uncertainties.

One possible solution is to perform the BAO analysis in overlapping redshift slices. This on one hand guarantees the sufficiency of galaxy numbers in each subsample, on the other hand, it allows for a higher temporal resolution. In this work, we perform such a tomographic BAO analysis in Fourier space using the DR12 galaxy sample, and quantify the gain in dark energy studies.

This paper is structured as follows. In Section 2, we describe the BOSS DR12 galaxy catalogues used for our analysis, and in Section 3, we perform a Fisher matrix forecast on this sample to determine the redshift binning, and present the power spectrum measurements. We perform the BAO analysis in Section 4, and apply our measurement to dark energy studies in Section 5, before we conclude in Section 6.

2 THE BOSS DR12 COMBINED SAMPLE

The BOSS program covers near 10,000 square degrees of the sky using a 2.5 metre-aperture Sloan Foundation Telescope (Gunn et al. 2006) at the Apache Point Observatory (APO) in New Mexico. The BOSS team has obtained spectra of more than 1.5 million galaxies brighter than $i = 19.9$ and approximately 170,000 new quasars

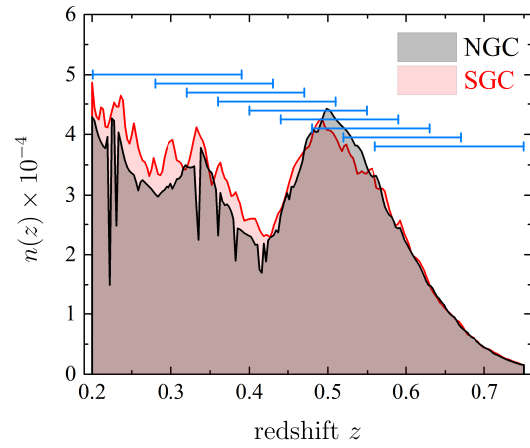


Figure 2. The volume number density of galaxies in units of $h^3 \text{Mpc}^{-3}$ in the NGC (black shaded) and SGC (red shaded). The nine horizontal overlapping bins illustrate our binning scheme.

with redshifts $2.1 \leq z \leq 3.5$ to a depth of $g < 22$ using the improved double-armed spectrographs in a wavelength range of $3,600 \text{\AA} < \lambda < 10,000 \text{\AA}$. The filter, spectrograph and pipeline of BOSS are described in Fukugita et al. (1996); Bolton et al. (2012); Smee et al. (2013).

The DR12 combined sample is a coherent combination of two distinct targets, LOWZ and CMASS. We refer the stellar-mass incompleteness of the LOWZ and CMASS samples to Leauthaud et al. (2016) and its impact on the clustering to Saito et al. (2016) and Rodríguez-Torres et al. (2016). The DR12 combined catalogue is created from the observational data using the pipeline described in Reid et al. (2016), in which the survey footprint, veto masks and survey systematics are taken into account to produce the data and random catalogues. The redshift range of this sample is $0.2 < z < 0.75$, and it contains $\sim 865,000$ and $\sim 330,000$ galaxies in the North Galactic Cap (NGC) ($\sim 5900 \text{ deg}^2$) and South Galactic Cap (SGC) ($\sim 2500 \text{ deg}^2$) respectively. The wedge plot (Fig. 1) visualises the DR12 sample³. The redshift distribution of the galaxies in the NGC and SGC is shown in Fig. 2. We refer the readers to Table 2 of Reid et al. (2016) for more details of the DR12 combined sample.

For each galaxy in the data catalogue, the following information is provided: the right ascension (RA), declination (DEC), redshift z and a set of weights including a FKP weight (Feldman et al. 1994) w_{FKP} , which is crucial to optimise the signal-to-noise ratio of power spectrum measurements, a systematic weight, w_{sys} to account for systematic effects from the contamination of stars and variations in seeing conditions, a redshift failure weight, w_{rf} to avoid using the galaxy without a robust redshift estimate, and a fibre collision weight, w_{fc} to correct for the clustering signal on small scales due to the fibre collision. With all the weights accounted for, each individual galaxy is counted as an effective number of,

$$w_{\text{T}} = w_{\text{FKP}} w_{\text{c}}; w_{\text{c}} = w_{\text{sys}} (w_{\text{fc}} + w_{\text{rf}} - 1) \quad (1)$$

More details of the weights are described in Ross et al. (2011); Anderson et al. (2014a); Ross et al. (2016).

³ For the purpose of visualisation, only 2% randomly selected galaxies are included in Fig. 1.

redshift bin index	redshift range	effective z	N_{NGC}	N_{SGC}	N_{tot}	σ_{D_A}/D_A	σ_H/H	σ_{D_V}/D_V
z bin 1	$0.20 < z < 0.39$	0.31	176,899	75,558	252,457	0.029	0.0705	0.024
z bin 2	$0.28 < z < 0.43$	0.36	194,754	81,539	276,293	0.028	0.0681	0.023
z bin 3	$0.32 < z < 0.47$	0.40	230,388	93,825	324,213	0.025	0.0616	0.021
z bin 4	$0.36 < z < 0.51$	0.44	294,749	115,029	409,778	0.023	0.0553	0.018
z bin 5	$0.40 < z < 0.55$	0.48	370,429	136,117	506,546	0.020	0.0502	0.017
z bin 6	$0.44 < z < 0.59$	0.52	423,716	154,486	578,202	0.019	0.0464	0.016
z bin 7	$0.48 < z < 0.63$	0.56	410,324	149,364	559,688	0.018	0.0441	0.015
z bin 8	$0.52 < z < 0.67$	0.59	331,067	121,145	452,212	0.018	0.0436	0.015
z bin 9	$0.56 < z < 0.75$	0.64	231,505	86,576	318,081	0.019	0.0418	0.014

Table 1. Statistics of the galaxies within nine overlapping redshift bins, and the corresponding Fisher forecast result for the BAO parameters.

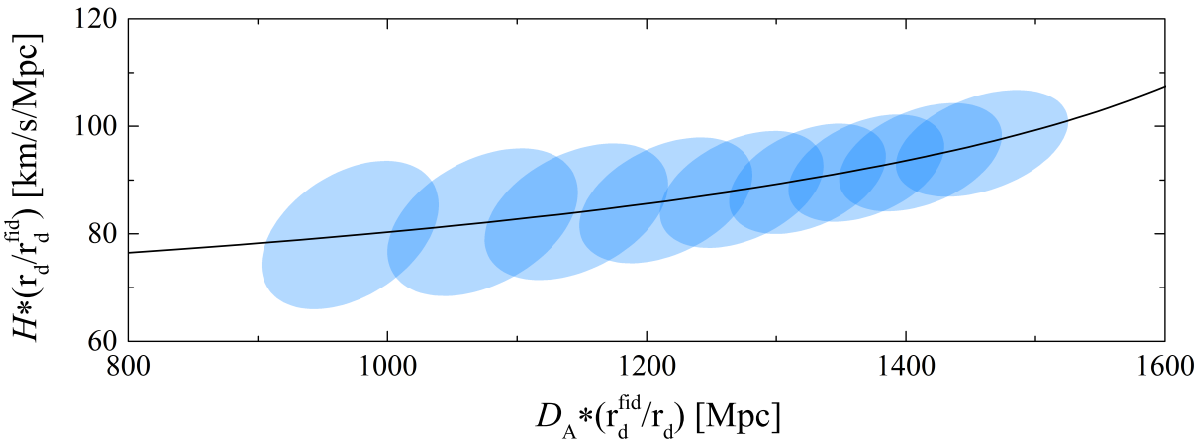


Figure 3. The 95% CL contour plots for $D_A * (r_d^{\text{fid}} / r_d)$ and $H * (r_d / r_d^{\text{fid}})$ derived from a Fisher matrix forecast for DR12 galaxies in nine redshift slices. For contours from left to right, the effective redshifts of galaxies used increase from $z_{\text{eff}} = 0.31$ to $z_{\text{eff}} = 0.64$. The black solid curve shows the prediction of the fiducial model used in this analysis.

For the clustering analysis, the auxiliary random catalogues, whose spatial and redshift distributions match those of data catalogues but without any clustering structure, are required. In this analysis, we use the random catalogues consisting of 50 times number of galaxies to reduce the sampling noise.

Since we only observe one realisation of the distribution of galaxies in the past lightcone, we need a large number of additional realisations, which can be obtained using numerical simulations, to estimate the data covariance matrix. In this work, we use the MultiDark PATCHY (MD-Patchy) mock catalogues (Kitaura et al. 2016b), which provide 2048 realisations of galaxy distribution matching the spatial and redshift distributions of the DR12 data sample. These galaxy mocks can accurately recover the input two-point and three-point statistics, and are sufficient for the calibration of data covariance matrix for this analysis.

Given RA, DEC and z , the Cartesian coordinates of the concerning galaxy, and hence the distances between galaxy pairs can be calculated, given a fiducial cosmology. It is true that the final BAO measurement is independent of the fiducial cosmology used for the redshift-distance conversion, and in the production of mock catalogues, we choose the same cosmological parameters used in the MD-Patchy mocks for convenience, *i.e.*,

$$\{\Omega_M, \Omega_b, \Omega_K, h, \sigma_8\} = \{0.307115, 0.0480, 0, 0.6777, 0.8288\} \quad (2)$$

which is consistent with the Planck cosmology (Planck Collaboration et al. 2015).

3 TOMOGRAPHIC BAO MEASUREMENTS

3.1 Preparations

To ensure a robust BAO distant measurement within each redshift slice while maximising the tomographic information, we employ a Fisher matrix forecast following the method developed in Seo & Eisenstein (2007). Using the k modes up to $0.3 h \text{ Mpc}^{-1}$ for the BAO analysis without the reconstruction process (Eisenstein et al. 2007a), we require that the precision of the isotropic BAO distance measurement within each redshift bin is better than 3%, while for the anisotropic BAO measurement, the precision on D_A and H within each bin is no worse than 4% and 8% respectively. We allow for the overlapping between neighbouring redshift bins to be 75% maximal, which well balances the redshift resolution and the complementarity of the information between overlapping bins. This yields a binning scheme visualised in Fig 2 and in Table 1. As shown, the entire sample is subdivided into nine bins, with the maximal overlapping to be 73%. The BAO projection result in Table 1 satisfies the requirement mentioned above, *i.e.*, the worst isotropic and anisotropic BAO distance measurement is predicted to be 2.4% (D_V), 2.9% (D_A) and 7% (H) respectively. The predicted 68 and 95% confidence level (CL) contours between D_A and H using galaxies in nine bins are shown in Fig. 3. The black solid curve illustrates the fiducial model.

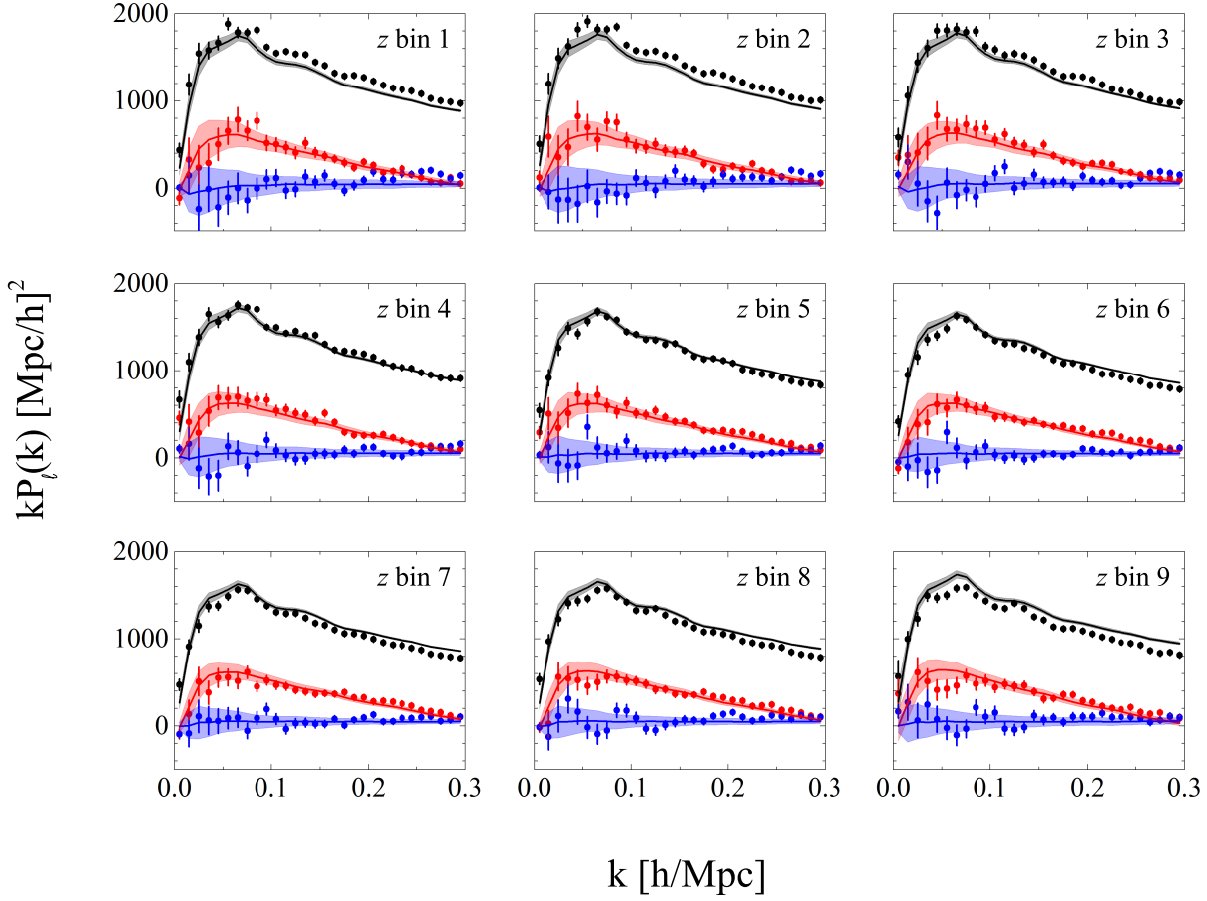


Figure 4. The power spectrum monopole (black), quadrupole (red) and hexadecapole (blue) measurements from the galaxy catalogue (data points) and from the MD-Patchy mock catalogue (shaded region) for the NGC. The solid curves are the average of all the mocks, and the error bars and error bands show the standard deviation at each k bin.

3.2 The interpolation scheme

The first step for the $P(k)$ multipole measurement is to assign the galaxies and randoms to a regular Cartesian grid, and choose an interpolation scheme to obtain a smoothed overdensity field for the Fourier analysis in next steps.

In this work, we embed the entire survey volume into a cubic box with $L = 5000 h^{-1}$ Mpc a side⁴, and the box is subdivided into $N_g^3 = 1024^3$ cubic cells. To obtain the smoothed overdensity field, an interpolation scheme is needed for the mass assignment. It is well known that the aliasing problem is inevitable in Fourier analysis, but choosing a suitable interpolation scheme (with corrections after the Fourier transformation; see discussions later) can largely reduce the aliasing to a negligible level at the scale for the BAO analysis.

The tradition interpolation schemes include the Nearest-Grid-Point (NGP), Cloud-in-Cell (CIC), Triangular-Shaped-Cloud (TSC) and so on. These correspond to the first, second and third

order B-spline interpolation. The higher order it is, the less level of aliasing survives after the correction (Sefusatti et al. 2015; Jing 2005).

Recently, Sefusatti et al. (2015) find that using the fourth-order B-spline, also called the Piecewise Cubic Spline (PCS) interpolation can suppress the aliasing effect to a level below 0.1% even at the Nyquist scale after the correction. In this work, we follow Sefusatti et al. (2015) and use the PCS interpolation to calculate the overdensity field on the grid, *i.e.*, we convolve the raw overdensity field with the following window function in real space,

$$W_\rho(s) = \begin{cases} \frac{1}{6}(4 - 6s^2 + 3|s|^3) & 0 \leq |s| < 1 \\ \frac{1}{6}(2 - |s|)^3 & 1 \leq |s| < 2 \\ 0 & \text{otherwise} \end{cases} \quad (3)$$

This means that the overdensity in each cell is contributed by galaxies and randoms in its $N_{\text{PCS}} = 5^3$ neighbouring cells⁵.

⁴ We have tested and found that a box with this size is sufficiently large to cover the entire survey volume.

⁵ For a reference, $N_{\text{NGP}} = 1$; $N_{\text{CIC}} = 2^3$, $N_{\text{TSC}} = 3^3$.

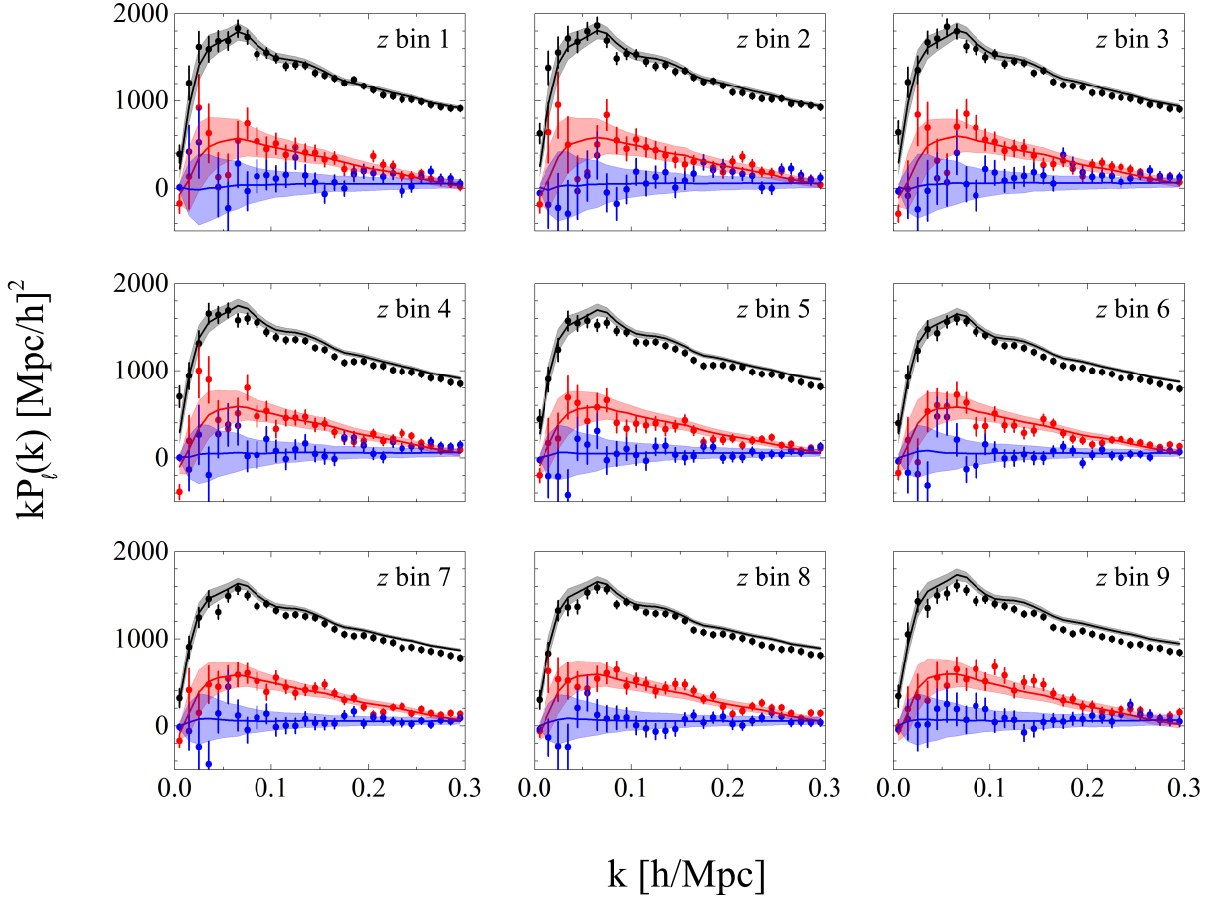


Figure 5. Same as Fig 4 but for the SGC.

After the interpolation, we obtain an overdensity field $\Delta(\mathbf{r})$,

$$\Delta(\mathbf{r}) \equiv \frac{w_T(\mathbf{r})}{\sqrt{N}} [n_G(\mathbf{r}) - \gamma n_R(\mathbf{r})] \quad (4)$$

where N is a normalisation factor which can be computed using the random catalogue (Feldman et al. 1994),

$$N = \gamma \sum_{i=1}^{N_R} n_G(\mathbf{r}_i) w_{\text{FKP}}^2(\mathbf{r}_i) \quad (5)$$

The summation here is over N_R samples in the random catalogue. The quantity w_T is the total weight for the concerning galaxy given in Eq (1), n_G and n_R are the number density at position \mathbf{r} of the galaxy and random catalogues respectively, γ is the ratio between the total sample numbers of the galaxy (N_G) and random (N_R) catalogues, *i.e.*, $\gamma = N_G/N_R$ and in this work $\gamma \sim 0.02$.

3.3 The estimator for $P_\ell(k)$

To measure the power spectrum multipole, we need to perform Fourier transformations of the overdensity field $\Delta(\mathbf{r})$ defined in Eq (4) (Yamamoto et al. 2006). Specifically, we need to calculate

the following quantity,

$$F_\ell(\mathbf{k}) \equiv \int d\mathbf{r} \Delta(\mathbf{r}) (\hat{\mathbf{k}} \cdot \hat{\mathbf{r}})^\ell e^{i\mathbf{k} \cdot \mathbf{r}} \quad (6)$$

for every \mathbf{k} mode. This integral was recently found to be evaluable using Fast Fourier Transformations (FFTs) (Bianchi et al. 2015; Scoccimarro 2015) instead of the expensive direct summation. We use the CAPSS package⁶ which requires the FFTW library⁷ to perform the Fourier transformations to obtain F_0 , F_2 and F_4 , which is the ingredient for the measurement of the monopole, quadrupole and hexadecapole moments of the galaxy power spectrum in redshift space.

Given $F_\ell(\mathbf{k})$, the power spectrum moments can be calculated

⁶ Cosmological Analysis Package for Spectroscopic Surveys (CAPSS) is a code package developed by Gong-Bo Zhao. CAPSS is written in Fortran 90, and can be used for the measurement of galaxy power spectrum and correlation function multipoles. CAPSS is used for all the BAO analysis in this work.

⁷ Publicly available at <http://www.fftw.org/>

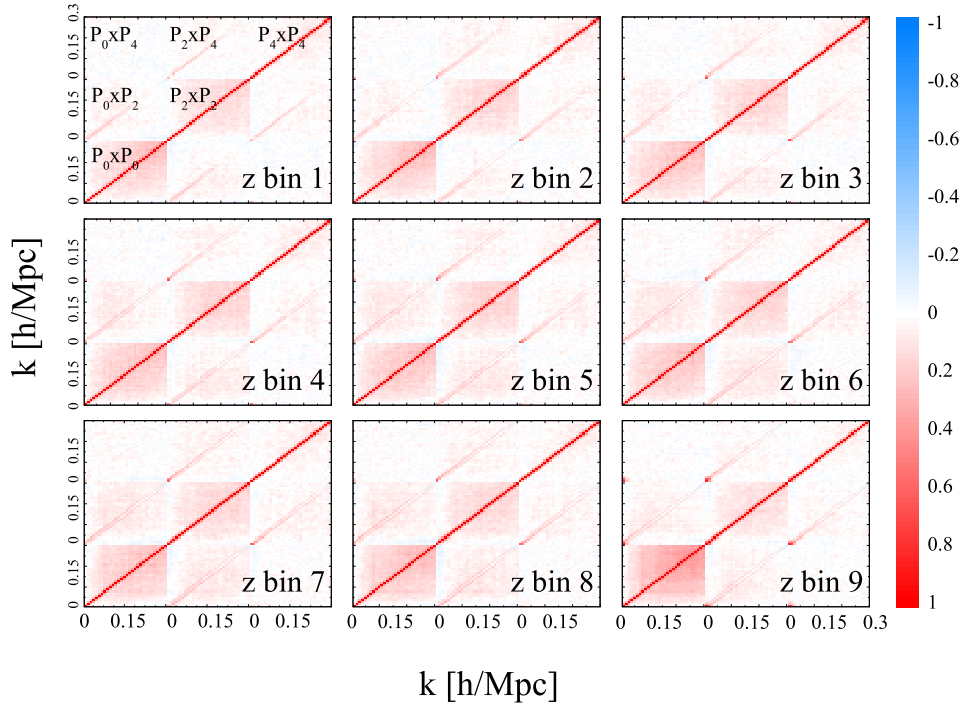


Figure 6. The correlation matrix of $P_\ell(k)$ for the galaxies in the NGC.

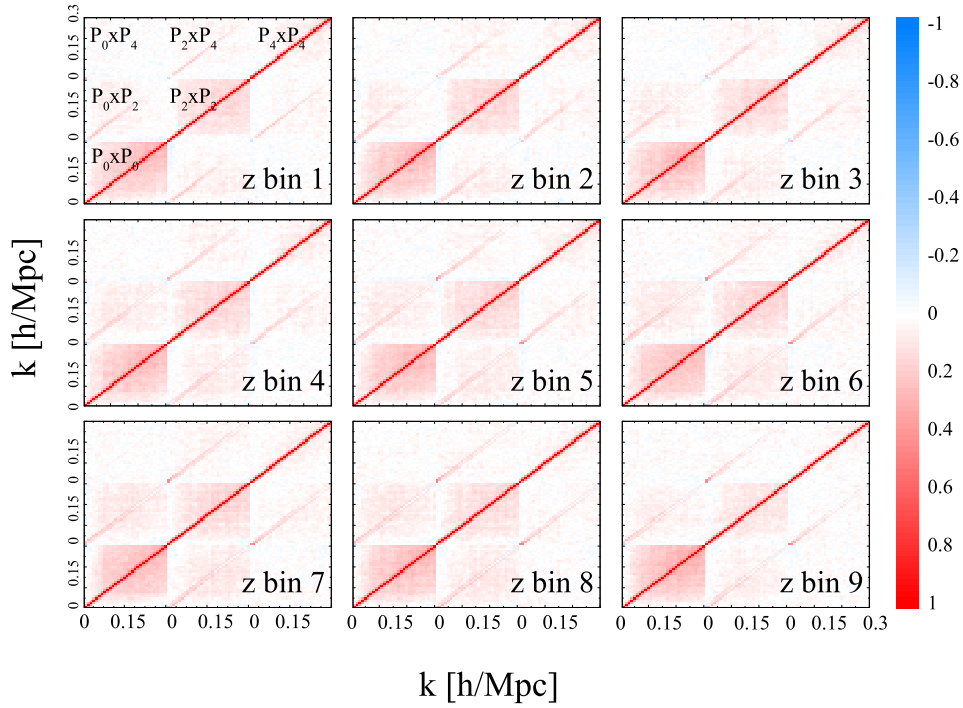


Figure 7. Same as Fig 6 but for the SGC.

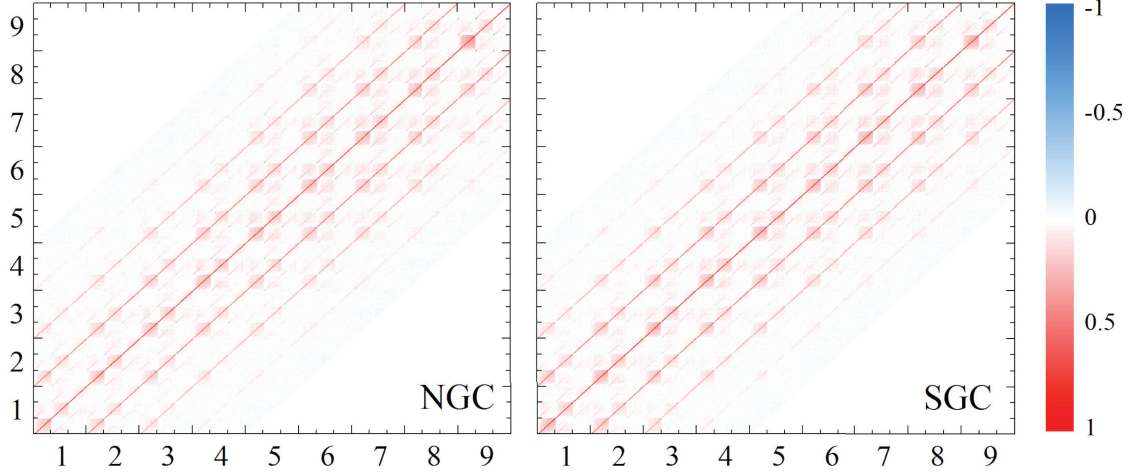


Figure 8. The full correlation matrix of $P_\ell(k)$ among nine redshift slices for the galaxies in the NGC (left) and in the SGC (right).

as,⁸,

$$\hat{P}_0(k) = \int \frac{d\Omega_k}{4\pi} [F_0(\mathbf{k})F_0^*(\mathbf{k})] - S \quad (7)$$

$$\hat{P}_2(k) = \frac{15}{2} \int \frac{d\Omega_k}{4\pi} [F_0(\mathbf{k})F_2^*(\mathbf{k})] - \frac{5}{2} [\hat{P}_0(k) + S] \quad (8)$$

$$\hat{P}_4(k) = \frac{315}{8} \int \frac{d\Omega_k}{4\pi} [F_0(\mathbf{k})F_4^*(\mathbf{k})] - \frac{9}{2} \hat{P}_2(k) - \frac{63}{8} [\hat{P}_0(k) + S] \quad (9)$$

where S is the shot noise term, which can be calculated as,

$$S = \sum_{i=1}^{N_G} \left[\zeta \frac{w_T^2}{w_{\text{fc}} + w_{\text{rf}} - 1} + (1 - \zeta) w_T^2 \right] + \gamma^2 \sum_{i=1}^{N_R} w_{\text{FKP}}^2 \quad (10)$$

The quantity ζ is the probability that a close pair of galaxies corrected by the fibre collision weight is a true pair. We set ζ to be 0.5 following the study in [Guo et al. \(2012\)](#). Note that for brevity, we have dropped the dependence of all the weights on location \mathbf{r}_i for the i th galaxy or random sample in Eq (10).

As mentioned earlier, the aliasing problem exists for all FFT-related manipulations, and it must be corrected for, especially close to the Nyquist scale. Here we follow [Jing \(2005\)](#) to correct for the aliasing effect analytically, *i.e.*, we divide each \mathbf{k} mode by the fol-

lowing correction factor for the PCS interpolation,

$$C(\mathbf{k}) = \prod_{i=1}^3 \left[1 - \frac{4}{3} \sin^2 \left(\frac{\pi k_i}{2k_N} \right) + \frac{2}{5} \sin^4 \left(\frac{\pi k_i}{2k_N} \right) - \frac{4}{315} \sin^6 \left(\frac{\pi k_i}{2k_N} \right) \right] \quad (11)$$

where i runs over three dimensions, and k_N is the Nyquist scale, $k_N = \pi N_g / L$ which is $\sim 0.64 h \text{ Mpc}^{-1}$ in our case. After the anti-aliasing correction, the level of aliasing is negligible ($< 0.1\%$) on scales of interest ($k < 0.3 h \text{ Mpc}^{-1}$) of our analysis.

3.4 The result of the $P_\ell(k)$ measurement

The measurement of $P_0(k)$, $P_2(k)$ and $P_4(k)$ for the galaxies in nine redshift slices in the NGC and SGC are shown as data points in Figs 4 and 5 respectively. Our measurement is in 30 k bins linearly spaced between $k = 0$ to $k = 0.3 h \text{ Mpc}^{-1}$. To quantify the uncertainty, we perform the same measurement on the MD-Patchy mocks, and compute the mean (shown as solid curves) and standard deviation (shown as error bars and shaded error bands) of the $P_\ell(k)$ measured in each k bin of the 2048 mocks. We find that although the measurements in the NGC and SGC are in general consistent with each other, an offset exists. This may be due to the slightly different selections used for the observations in two hemispheres. For more details of the discussion on the NGC-SGC discrepancy, we refer the readers to the companion papers of [Alam et al. \(2016\)](#); [Beutler et al. \(2016a\)](#); [Grieb et al. \(2016\)](#).

⁸ The formulae presented here are an rearrangement of the original ones in [Bianchi et al. \(2015\)](#) to improve efficiency and to save memory by minimising large matrix operations.

3.5 The data covariance matrix

The covariance between the i th k bin of the ℓ th order multipole in the m th redshift bin, and the j th k bin of the ℓ' th order multipole in the n th redshift bin can be calculated as follows,

$$C_{ij,mn}^{\ell,\ell'} = \frac{1}{N_{\text{mock}} - 1} \sum_{q=1}^{N_{\text{mock}}} [P_{\ell}^q(k_i, z_m) - \bar{P}_{\ell}(k_i, z_m)] \times [P_{\ell'}^q(k_j, z_n) - \bar{P}_{\ell'}(k_j, z_n)], \quad (12)$$

where the overbars denote the average value, *i.e.*,

$$\bar{P}_{\ell}(k_i, z_m) = \frac{1}{N_{\text{mock}}} \sum_{q=1}^{N_{\text{mock}}} P_{\ell}^q(k_i, z_m), \quad (13)$$

Here $N_{\text{mock}} = 2048$ is the number of mocks used.

Note that the estimated covariance matrix using mocks needs to be corrected for a bias using the Hartlap factor (Hartlap et al. 2007),

$$\tilde{C}_{ij}^{-1} = f_H C_{ij}^{-1}; f_H = \frac{N_{\text{mock}} - N_b - 2}{N_{\text{mock}} - 1}. \quad (14)$$

where N_b is the number of k bins. The correction is unbiased if the error distribution of the data is Gaussian, which is only true when $N_{\text{mock}} \gg N_b$ so that f_H is close to 1. For covariance between k bins within the same redshift slice, even if P_0, P_2 and P_4 are all included, $N_b = 90$, and $f_H = 0.956$. For the covariance between k bins in two different redshift slices, f_H reduces to 0.912, which is also sufficiently close to 1.

Figs 6 and 7 show the correlation matrix (the normalised covariance matrix so that all the diagonal elements are 1) for P_0, P_2, P_4 within the same redshift slice in the NGC and SGC respectively, and Fig 8 presents the full correlation matrix among all the redshift slices. The structure of these matrices is as follows:

- Multipoles with the same order positively correlate in general;
- Multipoles with different orders correlate more on the same scales;
- Multipoles in neighbouring redshift slices correlate, and the correlation generally decreases as the separation in redshift decreases;
- Multipoles in non-overlapping redshift slices do not correlate at all.

All of these observations make perfect sense intuitively.

4 THE BAO ANALYSIS

In this section, we shall measure the isotropic and anisotropic BAO signals from the $P(k)$ multipoles and the data covariance matrix. To begin with, we describe the theoretical models, *i.e.*, the BAO templates, for the analysis, followed by details of the fitting procedure and results.

4.1 The template for the isotropic BAO analysis

The isotropic BAO position is parametrised by the scale dilation parameter α ,

$$\alpha \equiv \frac{D_V(z)r_{d,\text{fid}}}{D_V^{\text{fid}}(z)r_d}, \quad (15)$$

where the volume distance $D_V(z)$ is defined in terms of the angular diameter distance $D_A(z)$ and the Hubble parameter, $H(z)$, *i.e.*,

$D_V(z) \equiv [cz(1+z)^2 D_A(z)^2 H^{-1}(z)]^{1/3}$, and r_d is the comoving sound horizon at the drag epoch. Quantities with the super- or subscript ‘fid’ are for the fiducial model parametrised by Eq (2). The template for the isotropic BAO is (Eisenstein et al. 2007b; Beutler et al. 2016a),

$$P_g(k) = P_{\text{nw}}(k) \left[1 + O(k)e^{-k^2 \Sigma_{\text{NL}}^2/2} \right] \quad (16)$$

$$P_{\text{nw}}(k) = B^2 P_{\text{nw,lin}}(k) F(k, \Sigma_s) \quad (17)$$

$$O(k) = \frac{P_{\text{lin}}(k)}{P_{\text{nw,lin}}(k)} - 1, \quad F(k) = \frac{1}{(1 + k^2 \Sigma_s^2/2)} \quad (18)$$

where $P_{\text{lin}}(k)$ is the linear power spectrum calculated using CAMB (Lewis et al. 2000)⁹, $P_{\text{nw,lin}}$ is the linear power spectrum with the BAO feature removed (Eisenstein & Hu 1998), $F(k, \Sigma_s)$ is the velocity damping term to account for the small scale Fingers-of-God (FoG) effect, B is an overall constant for the effect of galaxy bias and redshift space distortions (RSD), Σ_{NL} quantifies the nonlinear damping scale of the oscillations. We fix Σ_{NL} to be $3.3 \text{ h}^{-1} \text{ Mpc}$, which is motivated by numeric simulations (Eisenstein et al. 2007c; Seo et al. 2015). The theoretical model for the monopole is,

$$P_0(k) = \left(\frac{r_s^{\text{fid}}}{r_s} \right)^3 \frac{1}{\alpha^3} P_g(k') + \frac{a_{01}}{k^3} + \frac{a_{02}}{k^2} + \frac{a_{03}}{k} + a_{04} + a_{05} k \quad (19)$$

where $k' = k/\alpha$. The polynomials are included here to account for systematic effects (Anderson et al. 2014a; Alam et al. 2016). Once the parameters $\alpha, B, \Sigma_s, a_{0i}$ are known, one can use Eq (19) to obtain a theoretical prediction for the monopole for the fitting.

4.2 The template for the anisotropic BAO analysis

The BAO feature can also be measured in both the transverse and radial directions, parametrised by α_{\perp} and α_{\parallel} respectively,

$$\alpha_{\perp} = \frac{D_A(z)r_d^{\text{fid}}}{D_A^{\text{fid}}(z)r_d}, \quad \alpha_{\parallel} = \frac{H^{\text{fid}}(z)r_d^{\text{fid}}}{H(z)r_d}. \quad (20)$$

The template for the anisotropic BAO is slightly more complicated than the isotropic case due to several l.o.s.-dependent effects. The template is (Eisenstein et al. 2007b; Beutler et al. 2016a),

$$P_g(k, \mu) = P_{\text{nw}}(k, \mu) \left\{ 1 + O(k)e^{-k^2 [\mu^2 \Sigma_{\parallel}^2 + (1 - \mu^2) \Sigma_{\perp}^2]/2} \right\} \quad (21)$$

where

$$P_{\text{nw}}(k, \mu) = B^2 (1 + \beta \mu^2)^2 P_{\text{nw,lin}}(k) F(k, \mu) \quad (22)$$

and

$$F(k, \mu) = \frac{1}{(1 + k^2 \mu^2 \Sigma_s^2/2)} \quad (23)$$

$$P_{\ell}(k) = \left(\frac{r_s^{\text{fid}}}{r_s} \right)^3 \frac{2\ell + 1}{2\alpha_{\perp}^2 \alpha_{\parallel}} \int_{-1}^1 d\mu P_g(k', \mu') \mathcal{L}_{\ell}(\mu) + \frac{a_{\ell 1}}{k^3} + \frac{a_{\ell 2}}{k^2} + \frac{a_{\ell 3}}{k} + a_{\ell 4} + a_{\ell 5} k \quad (24)$$

⁹ Available at <http://camb.info>

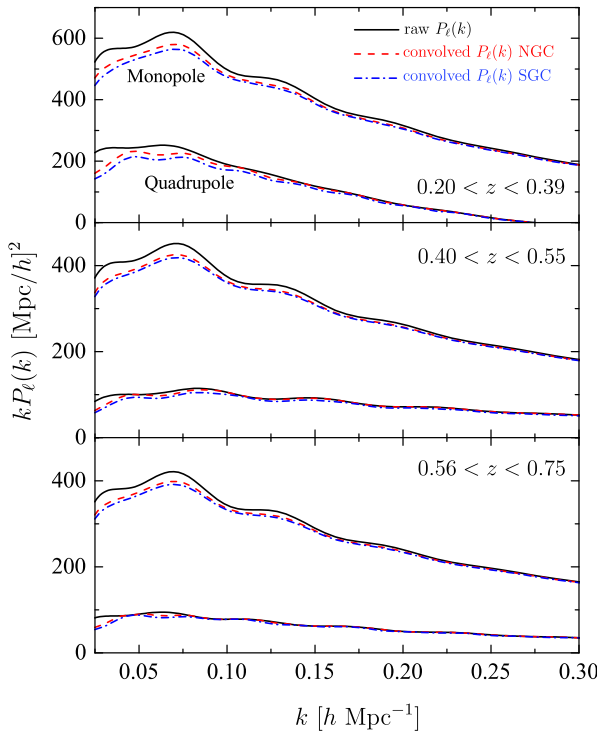


Figure 10. The theoretical $P_\ell(k)$ (black solid) and the convolved $P_\ell(k)$ with NGC (red dashed) and SGC (blue dash-dotted) window functions in three redshift slices.

where

$$\begin{aligned} k' &= \frac{k(1+\epsilon)}{\alpha} \{1 + \mu^2 [(1+\epsilon)^{-6} - 1]\}^{1/2} \\ \mu' &= \frac{\mu}{(1+\epsilon)^3} \{1 + \mu^2 [(1+\epsilon)^{-6} - 1]\}^{-1/2} \end{aligned} \quad (25)$$

where

$$\alpha = \alpha_\perp^{2/3} \alpha_\parallel^{1/3}, \quad 1 + \epsilon = \left(\frac{\alpha_\parallel}{\alpha_\perp}\right)^{1/3}. \quad (26)$$

Note that α is the isotropic BAO dilation, and ϵ is the warping factor. Eq (24) shows the Alcock-Paczynski effect, which is key to allow for the simultaneous determination of D_A and H using multipoles of $P(k)$ (Ballinger et al. 1996).

The $(1 + \beta\mu^2)^2$ term accounts for the RSD effect on large scales (Kaiser 1987), and exponential damping term becomes anisotropic in this case. We set $\Sigma_\parallel = 8 h^{-1} \text{Mpc}$ and $\Sigma_\perp = 4 h^{-1} \text{Mpc}$ motivated by simulations (Seo et al. 2015; Beutler et al. 2016a).

In this setup, once the parameter set $(\alpha_\perp, \alpha_\parallel, B, \beta, \Sigma_s, a_{\ell i})$ is known, one can predict $P_\ell(k)$ using Eq (24).

4.3 The survey window function

The theoretical model predictions derived using templates Eqs (19) or (24) cannot be directly compared to $P_\ell(k)$ measurements yet since the theoretical templates do not take into account the fact that the survey volume is irregular, and has a finite size. Ignoring these

facts can overestimate the power on large scales, which may yield a biased estimate on the BAO signal.

These effects can be accounted for by convolving the theoretical model prediction with the survey window function. The survey window function is generally anisotropic due to the irregular geometry of the survey volume, thus the window function multipoles need to be evaluated even for the isotropic BAO analysis.

Calculating the window function multipoles and performing the three-dimensional convolution with the theoretical model prediction can be technically challenging and cost expensive. Recently, Wilson et al. (2015) developed a new method for the window function evaluation and convolution. This method calculates the window function multipoles in configuration space based on a pair-counting using the random catalogue, correct for the windowing effect in real space, and then transform the result back to Fourier space using one-dimensional Hankel transformations. This is a very efficient and accurate method, thus we follow this approach in this analysis. We first compute the following pair counts in real space using a parallelised tree code in the CAPSS package,

$$Q_\ell(s) \propto \int_{-1}^1 d\mu RR(s, \mu) \mathcal{L}_\ell(\mu) \simeq \sum_i RR(s, \mu_i) \mathcal{L}_\ell(\mu_i) \quad (27)$$

The resultant Q_ℓ 's are shown in Fig 9. As shown, Q_ℓ vanishes on scales $\gtrsim 3000 h^{-1} \text{Mpc}$, and this scale is larger in the NGC than in the SGC due to large volume in the NGC. The higher multipoles contribute less in general, which guarantees a convergence result by keeping the first few Q_ℓ 's.

Given the Q_ℓ 's, we compute the *corrected* galaxy correlation function multipoles as follows (Beutler et al. 2016a,b; Wilson et al. 2015),

$$\begin{aligned} \hat{\xi}_0(s) &= \xi_0 Q_0 + \frac{1}{5} \xi_2 Q_2 + \frac{1}{9} \xi_4 Q_4 + \dots \\ \hat{\xi}_2(s) &= \xi_0 Q_2 + \xi_2 \left[Q_0 + \frac{2}{7} Q_2 + \frac{2}{7} Q_4 \right] \\ &\quad + \xi_4 \left[\frac{2}{7} Q_0 + \frac{100}{693} Q_4 + \frac{25}{143} Q_6 \right] + \dots \\ \hat{\xi}_4(s) &= \xi_0 Q_4 + \xi_2 \left[\frac{18}{35} Q_2 + \frac{20}{77} Q_4 + \frac{45}{143} Q_6 \right] \\ &\quad + \xi_4 \left[Q_0 + \frac{20}{77} Q_2 + \frac{162}{1001} Q_4 + \frac{20}{143} Q_6 + \frac{490}{2431} Q_8 \right] \\ &\quad + \dots \end{aligned} \quad (28)$$

where the ξ_ℓ 's are the correlation function multipoles converted from theoretical templates Eqs (19) or (24) using a one-dimensional Hankel transformation. Given the $\hat{\xi}_\ell$'s, we then perform a one-dimensional inverse Hankel transformation to obtain the window-convolved power spectrum, $P_\ell^{\text{conv}}(k)$, using the FFTlog package (Hamilton 2000)¹⁰.

The pre- and post-convoluted monopole and quadrupole for three redshift bins are shown in Fig 10. As expected, the window function reduces the large-scale powers due to the finite volume of the survey, and the damping effect from the SGC window function is larger due to the fact that the volume in the SGC is smaller than that in the NGC.

¹⁰ Available at <http://casa.colorado.edu/~ajsh/FFTLog/>

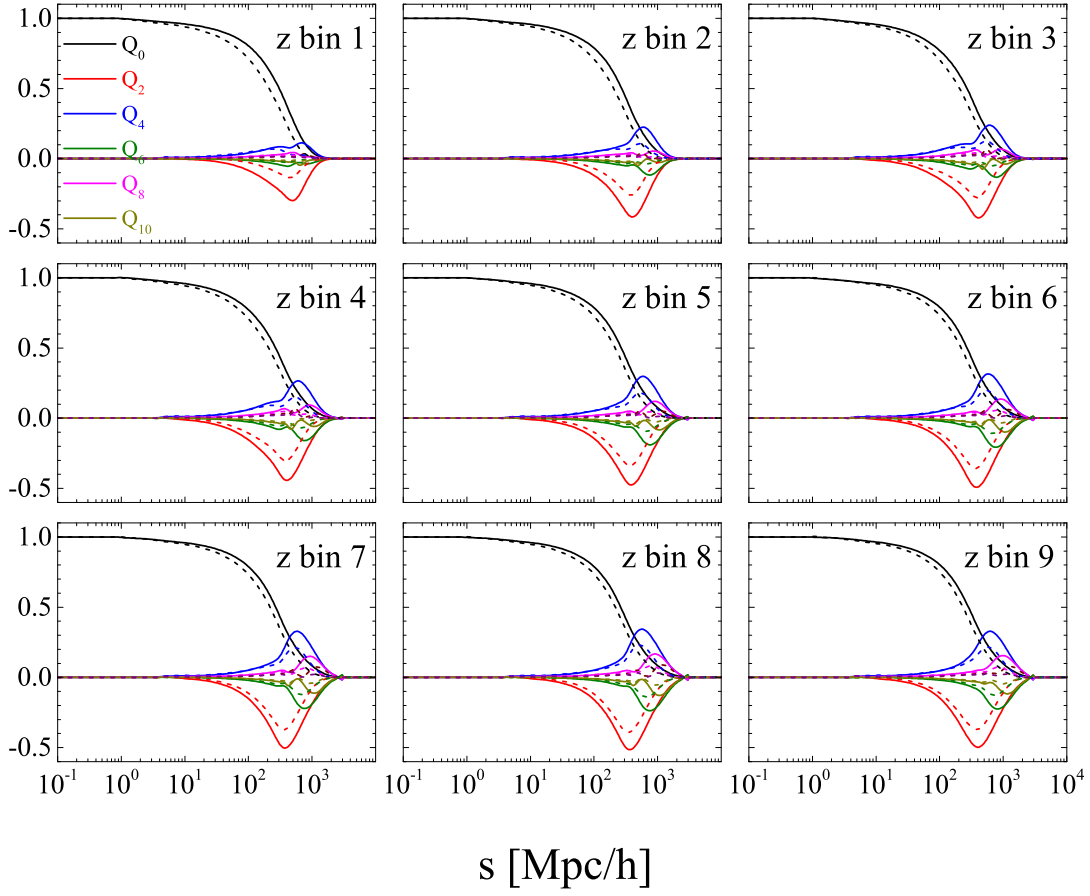


Figure 9. The normalised configuration space window function multipole $Q_\ell(s)$ calculated using pair counting of the random catalogues. The solid and dashed curves are for NGC and SGC respectively.

4.4 The MCMC BAO fitting

We constrain the BAO parameters for each redshift slices using a modified version of CosmoMC (Lewis & Bridle 2002)¹¹, which is a Markov Chain Monte Carlo (MCMC) engine. We sample the parameter space for the parameter vector \mathbf{p} by minimising the following χ^2 ,

$$\chi^2(\mathbf{p}) \equiv \sum_{i,j}^{\ell,\ell'} [P_\ell^{\text{conv}}(k_i, \mathbf{p}) - P_\ell(k_i)] F_{ij}^{\ell,\ell'} [P_{\ell'}^{\text{conv}}(k_j, \mathbf{p}) - P_{\ell'}(k_j)]$$

where $F_{ij}^{\ell,\ell'}$ is the inverse of the data covariance matrix. Note that when using both the NGC and SGC data for the constraint, we use two separate B parameters for the NGC and SGC to account for the offset discussed earlier. We analytically marginalise over the coefficients of polynomials in each MCMC step, *i.e.*, we calculate the optimal values of the coefficients given a set of parameters to minimise the χ^2 ,

$$\chi^2 = (\mathbf{D} + \mathbf{X})^T \mathbf{F} (\mathbf{D} + \mathbf{X}) \quad (29)$$

¹¹ Available at <http://cosmologist.info/cosmomc/>

where the residue vector \mathbf{D} is defined as

$$\mathbf{D}(k) \equiv P^{\text{data}}(k) - P^{\text{theo.}}(k) \quad (30)$$

and the polynomial vector \mathbf{X} is,

$$\mathbf{X} \equiv \mathbf{A} \cdot \mathbf{K} \quad (31)$$

where

$$\mathbf{K} \equiv \left(\frac{1}{k^3}, \frac{1}{k^2}, \frac{1}{k}, 1, k \right) \quad (32)$$

Given \mathbf{D} and \mathbf{F} at each MCMC step, our aim is to analytically determine the coefficients vector \mathbf{A} to minimise χ^2 . To do this, we expand Eq (29), and setting $\partial\chi^2/\partial\mathbf{X} = 0$ yields,

$$\mathbf{A}^T = (\mathbf{K} \mathbf{F} \mathbf{K}^T)^{-1} \mathbf{K} \mathbf{F} \mathbf{D} \quad (33)$$

This procedure can avoid fitting these weakly constrained nuisance parameters, making the MCMC chains much easier to converge.

After the MCMC chains converge, we perform statistics on the chain elements to obtain the posterior distribution of each parameters, and the correlation among parameters. Note that the data covariance matrix estimated from the finite mocks inevitably has

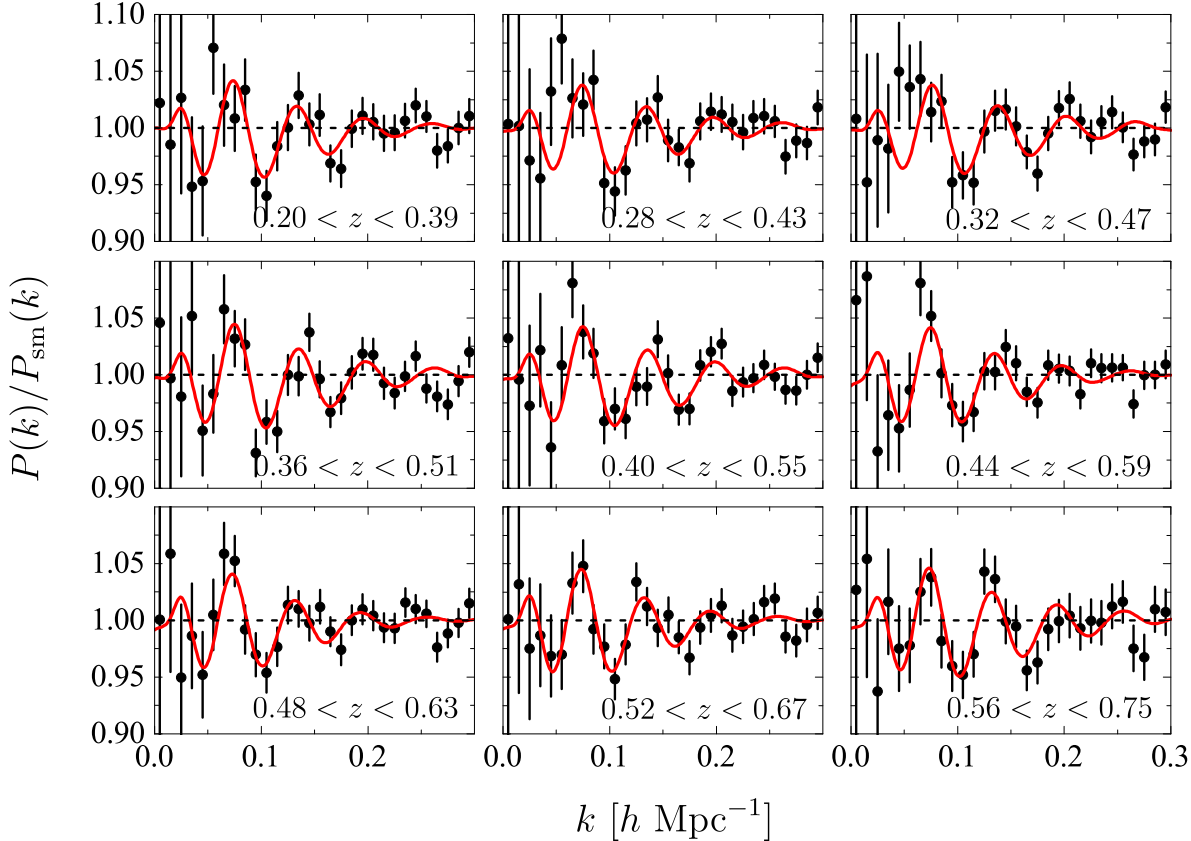


Figure 11. An overplot of the measured $P(k)$ monopole using the galaxies in the NGC (data with error bars) and the best fit model (red solid), rescaled by the best fit model without the BAO feature.

errors, which have propagated into the errors of parameters. To correct, we follow Percival et al. (2014) to rescale the variance of each parameter by

$$M = \sqrt{\frac{1 + B(N_b - N_p)}{1 + A + B(N_p + 1)}} \quad (34)$$

where N_p is the number of parameters, and

$$A = \frac{2}{(N_{\text{mock}} - N_b - 1)(N - N_b - 4)},$$

$$B = \frac{N_{\text{mock}} - N_b - 2}{(N_{\text{mock}} - N_b - 1)(N_{\text{mock}} - N_b - 4)}. \quad (35)$$

4.5 Mock tests

We first validate our pipeline by performing the BAO analysis on the MD-Patchy mocks. We fit the isotropic, and anisotropic BAO parameters to the average of 2048 mocks. The isotropic BAO test is shown in Table 2 and Fig 12 (red dashed curves for one-dimensional posterior distribution of α). As shown in the left part of Table 2, the mean value of α 's are consistent with 1, which is the input value of all the mocks, within 0.3σ in the worst case (for redshift bin z_9). This bias could be due to nonlinearities such as the mode-coupling effect on quasi-nonlinear scales (Padmanabhan

& White 2009), which can be approximately estimated analytically (Seo et al. 2008; Padmanabhan & White 2009). The expected shift in α in 9 redshift bins are shown in the $\Delta\alpha_{\text{MC}}$ column in Table 2, which is 0.17σ in the worst case (for redshift bin z_7). To account for this systematic effect conservatively, we include a systematic error budget on α by adding $\Delta\alpha_{\text{MC}}$ and the shift of the mean α from 1 in quadrature, for the BAO measurements using the galaxy sample, which will be presented later.

The mock test results for anisotropic BAO are shown in Table 3 and in Fig 13, where the result using monopole and quadrupole ($P_0 + P_2$), and monopole, quadrupole, and hexadecapole separately ($P_0 + P_2 + P_4$). As shown, the hexadecapole improves the constraint in all redshift bins, *i.e.*,

- It shrinks the statistical error budget by $9 - 15\%$ for $\alpha_{||}$, and $8 - 11\%$ for α_{\perp} ;
- It generally makes the mean value of both $\alpha_{||}$ and α_{\perp} more consistent with unity;
- It reduces the degeneracy between $\alpha_{||}$ and α_{\perp} by $18 - 32\%$.

This means that the hexadecapole from DR12 sample is indeed informative for BAO studies. It is true that given the level of uncertainty of $P_4(k)$, the BAO feature is barely visible. However, it can improve the global fitting by providing constraints on the amplitude parameters B and the RSD parameter β , thus reduce the

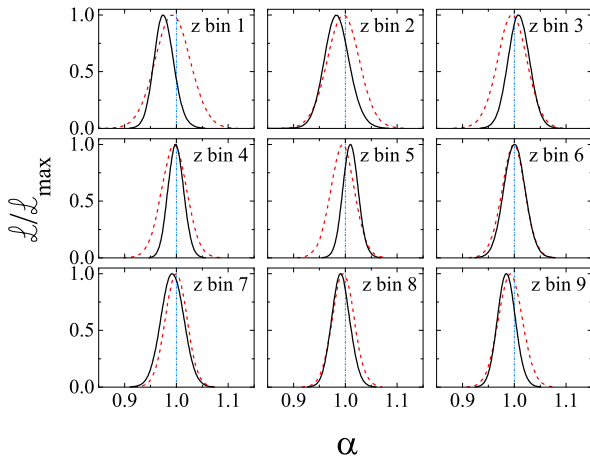


Figure 12. The one-dimensional posterior distribution of the isotropic α derived from the observations (black solid) and mock catalogues (red dashed) respectively. The blue dash-dotted lines show $\alpha = 1$ for a reference.

degeneracy between $\alpha_{||}$ and α_{\perp} , and improve their constraints indirectly. Given the importance of the hexadecapole, we shall include it in all the analysis in this work unless otherwise mentioned.

We quantify the systematic error budget similarly to the isotropic BAO case, *i.e.*, the systematic error is estimated using the quadrature addition between the bias caused by the mode-coupling effect, and the shift of mean $\alpha_{||}$ and α_{\perp} from unity. The mode-coupling bias is taken to be $\Delta\alpha_{||}^{\text{MC}} = 0.001$ and $\Delta\alpha_{\perp}^{\text{MC}} = 0.009$ (Ross et al. 2016). This yields a $0.15 - 0.76\%$ systematic error on $\alpha_{||}$, and $0.09 - 0.1\%$ on α_{\perp} .

In summary, we validate our pipeline using mock tests, namely, the bias introduced by the pipeline is sufficiently small compared to the statistical error in all cases, and the bias is accounted for by the systematic error budget.

4.6 BAO measurements from DR12 sample

In this section, we shall apply our BAO analysis pipeline on the DR12 sample, and present the main results of this paper.

4.6.1 Isotropic BAO measurements

The isotropic BAO fitting result is shown in the right part of Table 2 and in Figs 11 and 12 (black solid). Fig 11 displays the best-fit monopole and data points, divided by the smoothed power spectrum. As shown, the BAO signal is well extracted in all the redshift slices. From Table 2 and Fig 12, which shows the one-dimensional posterior distribution of α , in comparison to those measured from the mocks, we see that the isotropic BAO distance is determined at a precision of 1.5% to 3.4%, depending on the effective redshifts. We also notice that α in three redshift slices deviate from 1 at $\gtrsim 1\sigma$ level. This may suggest that the fiducial cosmology, which is the Λ CDM model with parameters listed in Eq (2), might be in tension with the DR12 galaxy sample. We shall explore this more in a companion paper (Zhao et al. 2016).

4.6.2 Anisotropic BAO measurements

The anisotropic BAO measurements are presented in Tables 4, Figs 16 to 19. Table 4 shows the constraint on $\alpha_{||}$ and α_{\perp} , D_A/r_d and $H r_d$ at nine effective redshifts with the correlation coefficients and the reduced χ^2 to quantify the goodness-of-fit. We can see that the anisotropic BAO distances in terms of D_A/r_d and $H r_d$ are measured to a precision of $1.8\% - 4.2\%$ and $3.7\% - 7.5\%$ respectively, depending on the effective redshifts. The reduced χ^2 is sufficiently close to unity in all cases, which means that the fitting result is as expected. We also notice that the α 's show deviation from 1 at $\gtrsim 1\sigma$ level, which is consistent with the result of the isotropic BAO measurement.

Fig 14 shows the contour plots between $\alpha_{||}$ and α_{\perp} using galaxies in the NGC (unfilled black) and NGC+SGC (filled blue). These results show that the BAO distances measured from the NGC and SGC are in general consistent with each other, and complementary. In the two-dimensional plane, we see the deviation from the fiducial model (shown as white crosses) at $\gtrsim 1\sigma$ level only in the fourth redshift slice.

Fig 15 shows the contour plots of D_A/r_d and $H r_d$, together with the prediction of the fiducial model. Comparing with Fig 3, we find that the degeneracy between D_A/r_d and $H r_d$ are consistent with the forecast, while the uncertainties are generally larger, especially for the first and last two bins. This is expected as it is well known that the Fisher forecast, which assumes the Gaussian distribution of parameters, and ignores the systematic effects in the catalogue, can underestimate the errors. Thus we only take the forecast result as a rough guidance for the analysis.

Fig 16 visualises the two-dimensional BAO ring in the third redshift slice. The quantity shown in the colours is the two-dimensional power spectrum, which is assembled from our measured P_0 , P_2 and P_4 , *i.e.*,

$$P(k, \mu) = \sum_{\ell=0,2,4} P_{\ell}(k) L_{\ell}(\mu) \quad (36)$$

To visualise the BAO ring, we divide $P(k, \mu)$ by the smoothed power spectrum $P_{\text{sm}}(k, \mu)$.

Fig 17 shows the constraints on the α 's as a function of redshift and in Fig 18, we compare our measurement to the companion paper performing the same tomographic BAO analysis in configuration space (Wang et al. 2016). Although the results are in general consistent with each other within the 68% CL bound, the difference exists especially for $\alpha_{||}$ and α_{\perp} , which may be explained as follows,

- Wang et al. (2016) uses the monopole and quadrupole of the correlation function, while in this work we use the hexadecapole in addition. As discussed in Sec. 4.5, the hexadecapole is sufficiently informative to improve the BAO constraint, and to reduce the theoretical systematics;

- Although the correlation function and power spectrum have the same information of BAO in the ideal case (*i.e.*, a survey with an infinite volume without shot noise), a difference is expected for a realistic galaxy survey.

The companion paper Salazar-Albornoz et al. (2016) performs a similar tomographic BAO analysis, but using different observables and pipeline. Salazar-Albornoz et al. (2016) measured the projected two-dimensional angular correlation functions instead in a larger number of redshift slices, and obtained both the BAO and RSD parameters. This method avoids the necessity of choosing a fiducial cosmological model to convert redshifts to distances, which

Table 2. The constraint on the isotropic BAO parameters α and D_V , from the mocks (left) and the galaxy catalogues (right). For quantities with double error bars, the first and second shows the statistical and systematical error budget respectively.

z bins	$\Delta\alpha^{\text{MC}}$	Mock catalogue		Galaxy catalogue		χ^2/dof
		α	α	$\left(\frac{D_V}{\text{Mpc}}\right)$	$\left(\frac{r_d^{\text{fid}}}{r_d}\right)$	
z_1	0.0040	0.9925 ± 0.0346	$0.9765 \pm 0.0190 \pm 0.0085$	$1208.36 \pm 23.51 \pm 10.30$	$43/51$	
z_2	0.0039	0.9960 ± 0.0308	$0.9822 \pm 0.0332 \pm 0.0056$	$1388.36 \pm 46.93 \pm 7.790$	$59/51$	
z_3	0.0039	0.9956 ± 0.0283	$1.0088 \pm 0.0205 \pm 0.0058$	$1560.06 \pm 31.70 \pm 9.120$	$67/51$	
z_4	0.0038	0.9955 ± 0.0245	$0.9992 \pm 0.0149 \pm 0.0059$	$1679.88 \pm 25.05 \pm 9.850$	$69/51$	
z_5	0.0037	0.9945 ± 0.0231	$1.0102 \pm 0.0149 \pm 0.0066$	$1820.44 \pm 26.85 \pm 12.04$	$69/51$	
z_6	0.0036	0.9979 ± 0.0221	$1.0003 \pm 0.0204 \pm 0.0041$	$1913.54 \pm 39.03 \pm 7.930$	$50/51$	
z_7	0.0035	0.9994 ± 0.0206	$0.9923 \pm 0.0216 \pm 0.0035$	$2001.91 \pm 43.58 \pm 7.050$	$56/51$	
z_8	0.0034	0.9958 ± 0.0209	$0.9914 \pm 0.0175 \pm 0.0054$	$2100.43 \pm 37.08 \pm 11.29$	$51/51$	
z_9	0.0032	0.9926 ± 0.0229	$0.9852 \pm 0.0171 \pm 0.0081$	$2207.51 \pm 38.32 \pm 17.80$	$50/51$	

Table 3. The constraint on the anisotropic BAO signal, α_{\perp} and α_{\parallel} , and their correlation coefficient, $r_{\perp\parallel}$.

z bins	Mock catalogue ($P_0 + P_2$)			Mock catalogue ($P_0 + P_2 + P_4$)		
	α_{\parallel}	α_{\perp}	$r_{\parallel\perp}$	α_{\parallel}	α_{\perp}	$r_{\parallel\perp}$
z_1	0.9841 ± 0.0855	1.0023 ± 0.0459	-0.44	0.9928 ± 0.0768	0.9970 ± 0.0416	-0.30
z_2	0.9985 ± 0.0861	0.9990 ± 0.0449	-0.49	1.0046 ± 0.0763	0.9952 ± 0.0405	-0.35
z_3	1.0008 ± 0.0796	1.0024 ± 0.0410	-0.49	1.0072 ± 0.0705	0.9991 ± 0.0370	-0.37
z_4	0.9942 ± 0.0735	1.0010 ± 0.0344	-0.49	1.0047 ± 0.0641	0.9976 ± 0.0317	-0.38
z_5	0.9948 ± 0.0702	1.0001 ± 0.0324	-0.50	1.0020 ± 0.0598	0.9977 ± 0.0295	-0.38
z_6	0.9972 ± 0.0683	1.0021 ± 0.0303	-0.51	1.0069 ± 0.0581	0.9996 ± 0.0269	-0.36
z_7	1.0034 ± 0.0628	1.0008 ± 0.0296	-0.50	1.0075 ± 0.0548	0.9996 ± 0.0274	-0.39
z_8	0.9971 ± 0.0659	0.9990 ± 0.0329	-0.55	1.0049 ± 0.0582	0.9962 ± 0.0296	-0.45
z_9	0.9913 ± 0.0654	0.9994 ± 0.0354	-0.51	0.9989 ± 0.0598	0.9965 ± 0.0324	-0.40

can reduce theoretical systematics in principle, but may be subject to the issue of information loss due to the projection effect, unless a large number of tomographic bins are used (Asorey et al. 2012).

Companion papers Alam et al. (2016); Beutler et al. (2016a); Ross et al. (2016); Grieb et al. (2016); Sanchez et al. (2016b) perform the BAO measurements using the same galaxy catalogue but in three redshift slices of $0.2 < z < 0.5$, $0.4 < z < 0.6$ and $0.5 < z < 0.75$. We compare our result to the ‘DR12 Consensus’ result presented in Alam et al. (2016) since it is coherently compiled from a range of BAO measurements mentioned above, thus we expect it to be least affected by systematics.

An overplot of the DR12 Consensus measurement and ours is shown in Fig 19, with the Planck2015 measurement (mean and 68, 95% CL errors) shown in blue bands, where $D_M \equiv D_A(1+z)$. A direct one-to-one comparison is impossible simply because our measurements are performed at six additional effective redshifts. The only way for the comparison is to downgrade the redshift resolution of our measurement into three effective redshifts. We follow the procedure presented in Sanchez et al. (2016a) for the data compression, and find an agreement within 68% CL. The comparison is also illustrated in Table 9 and Fig 13 in Alam et al. (2016).

In order to use our 9-bin tomographic BAO measurement for cosmology, the correlation between redshift bins needs to be quantified. For this purpose, we jointly fit the anisotropic BAO distances in all pairs of overlapping redshift bins, *i.e.*, jointly fit $\alpha_{\parallel}(z_i), \alpha_{\parallel}(z_j), \alpha_{\perp}(z_i), \alpha_{\perp}(z_j)$ with other nuisance parameters marginalised over where $i = 1 : 8$; $j = i + 1 : 9$, and calcu-

late the correlation matrix using the MCMC chain elements. The resultant correlation matrix is shown in Fig 20. As shown, the correlation of the same quantity between redshift bins is positive, and decreases as the redshift separation increases, which is expected. The electronic dataset of measurements presented in this work is available online at https://sdss3.org//science/boss_publications.php.

5 DARK ENERGY IMPLICATIONS

In this section, we utilise our tomographic BAO measurements to constrain the equation-of-state (EoS) function of dark energy, w , parametrised in the CPL form, (Chevallier & Polarski 2001; Linder 2003),

$$w(a) = w_0 + w_a(1-a). \quad (37)$$

where a is the scale factor of the Universe. We constrain w_0, w_a together with other basic cosmological parameters including the physical baryon energy density $\Omega_b h^2$, the physical cold dark matter energy density $\Omega_c h^2$, the ratio between the angular diameter distance and sound horizon at recombination Θ_s , the amplitude and power index of the primordial power spectrum A_s and n_s respectively.

Besides the BAO data, we combine with the CMB measurement from the Planck mission (Planck Collaboration et al. 2015) including the auto- and cross-angular power spectrum of the tem-

Table 4. The mean value with 68% statistical error (first error bar) and systematic error (second error bar) of the anisotropic BAO signal, α_{\perp} , α_{\parallel} , Hr_d and D_A/r_d , the corresponding correlation coefficient, and the reduced χ^2 to quantify the goodness-of-fit.

z bins	α_{\parallel}	α_{\perp}	$r_{\parallel\perp}$	$\left(\frac{H}{\text{km s}^{-1} \text{Mpc}^{-1}}\right) \left(\frac{r_d}{r_d^{\text{fid}}}\right)$	$\left(\frac{D_A}{\text{Mpc}}\right) \left(\frac{r_d^{\text{fid}}}{r_d}\right)$	χ^2/dof
z_1	$1.0214 \pm 0.0522 \pm 0.0073$	$0.9592 \pm 0.0402 \pm 0.0095$	-0.43	$78.30 \pm 4.07 \pm 0.57$	$931.420 \pm 39.42 \pm 8.840$	150/144
z_2	$1.0687 \pm 0.0694 \pm 0.0047$	$0.9751 \pm 0.0322 \pm 0.0102$	-0.23	$77.20 \pm 5.30 \pm 0.36$	$1047.04 \pm 33.65 \pm 10.68$	156/144
z_3	$1.0583 \pm 0.0539 \pm 0.0073$	$0.9878 \pm 0.0280 \pm 0.0090$	-0.35	$79.72 \pm 4.27 \pm 0.58$	$1131.34 \pm 34.06 \pm 10.23$	180/144
z_4	$1.0751 \pm 0.0396 \pm 0.0048$	$0.9785 \pm 0.0172 \pm 0.0093$	-0.30	$80.29 \pm 2.96 \pm 0.39$	$1188.78 \pm 20.90 \pm 11.07$	184/144
z_5	$1.0432 \pm 0.0389 \pm 0.0022$	$0.9985 \pm 0.0189 \pm 0.0093$	-0.25	$84.69 \pm 3.21 \pm 0.19$	$1271.43 \pm 24.03 \pm 11.81$	173/144
z_6	$0.9865 \pm 0.0743 \pm 0.0070$	$1.0093 \pm 0.0202 \pm 0.0090$	-0.37	$91.97 \pm 6.85 \pm 0.64$	$1336.53 \pm 26.72 \pm 12.04$	149/144
z_7	$0.9526 \pm 0.0710 \pm 0.0076$	$1.0116 \pm 0.0205 \pm 0.0090$	-0.26	$97.30 \pm 7.16 \pm 0.74$	$1385.47 \pm 28.04 \pm 12.48$	165/144
z_8	$0.9735 \pm 0.0528 \pm 0.0050$	$1.0085 \pm 0.0217 \pm 0.0098$	-0.35	$97.07 \pm 5.24 \pm 0.49$	$1423.43 \pm 30.66 \pm 13.91$	144/144
z_9	$0.9931 \pm 0.0474 \pm 0.0015$	$0.9932 \pm 0.0378 \pm 0.0097$	-0.56	$97.70 \pm 4.58 \pm 0.15$	$1448.81 \pm 55.12 \pm 13.99$	138/144

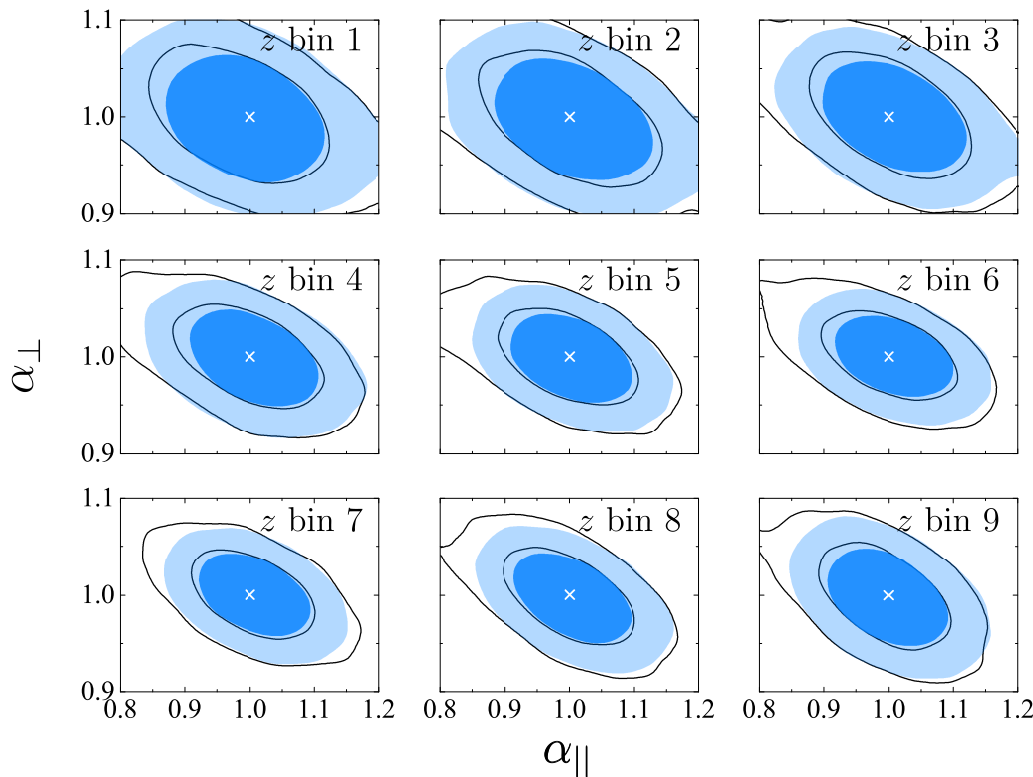


Figure 13. The 68 and 95% CL contour plots for α_{\parallel} and α_{\perp} using $P(k)$ multipoles (black unfilled contours: $P_0 + P_2$; blue filled contours: $P_0 + P_2 + P_4$) measured from the MD-PATCHY mock catalogue in nine redshift slices. The unfilled black and filled blue contours are results using galaxies in the NGC, and all galaxies in the catalogue respectively. The white cross in each panel illustrates the fiducial model ($\alpha_{\parallel} = \alpha_{\perp} = 1$).

perature and polarisation fluctuations of the CMB photons, the supernovae Type Ia sample of JLA (Betoule et al. 2014), the galaxy power spectra from the WiggleZ survey (Blake et al. 2011), and the tomographic measurement of the weak lensing shear angular power spectra provided by the CFHTLenS team (Heymans et al. 2013). We pay particular attention to the dark energy perturbations when $w(a)$ crosses the -1 boundary (Zhao et al. 2005; Fang et al.

2008). We use CosmoMC to sample the 7-dimensional parameter space and perform statistical analysis on the Markov chains after the perfect convergence of the sampling process.

The result is visually shown in Fig 21, where the 68 and 95% CL contours of w_0, w_a are plotted for two different data combinations ('Base' means a data combination of Planck, JLA, WiggleZ and CFHTLenS). The constraints using our nine-bin tomographic

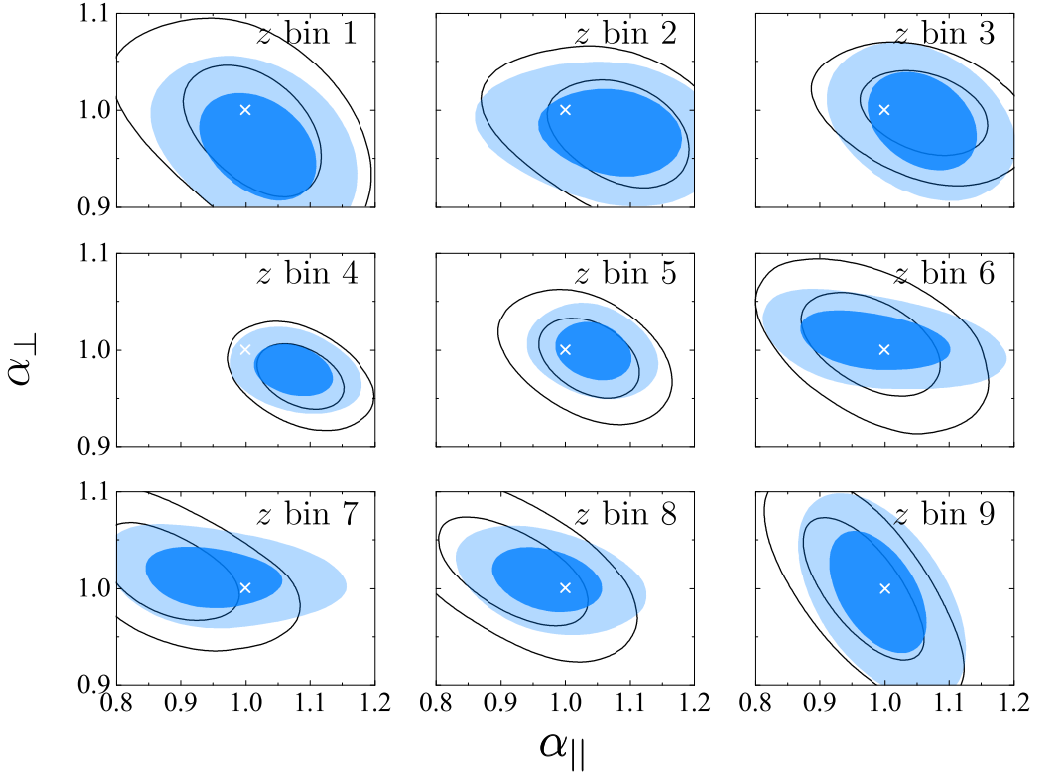


Figure 14. The 68 and 95% CL contour plots for α_{\parallel} and α_{\perp} using $P(k)$ multipoles measured from the DR12 galaxy sample in nine redshift slices. The unfilled black and filled blue contours are results using galaxies in the NGC, and all galaxies in the catalogue respectively. The white cross in each panel illustrates the fiducial model ($\alpha_{\parallel} = \alpha_{\perp} = 1$).

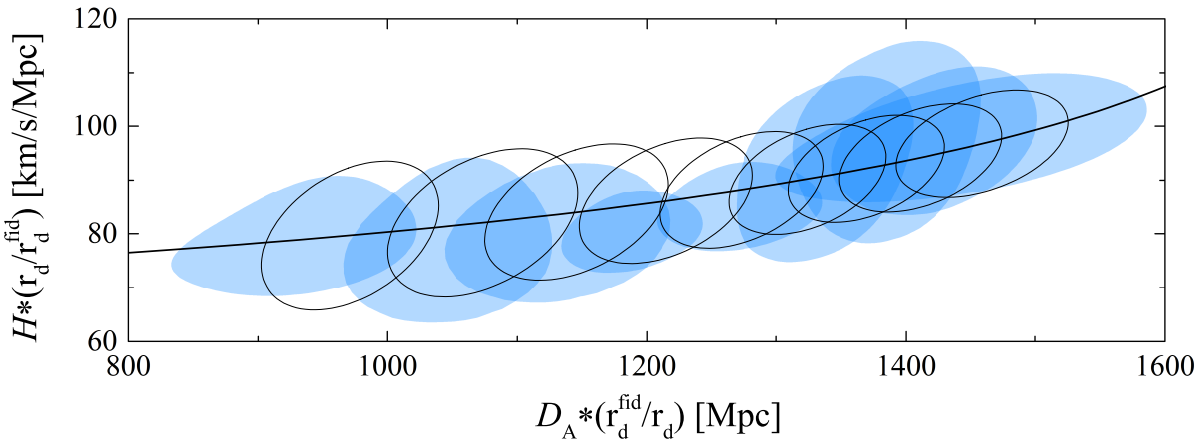


Figure 15. Shaded contours: the 95% CL contour plots for $D_A * (r_d^{\text{fid}}/r_d)$ and $H * (r_d/r_d^{\text{fid}})$ derived from DR12 galaxies in nine redshift slices; black unfilled contours: the Fisher matrix forecast. For contours from left to right, the effective redshifts of galaxies used increase from $z_{\text{eff}} = 0.31$ to $z_{\text{eff}} = 0.64$. The black solid curve shows the prediction of the fiducial model used in this analysis.

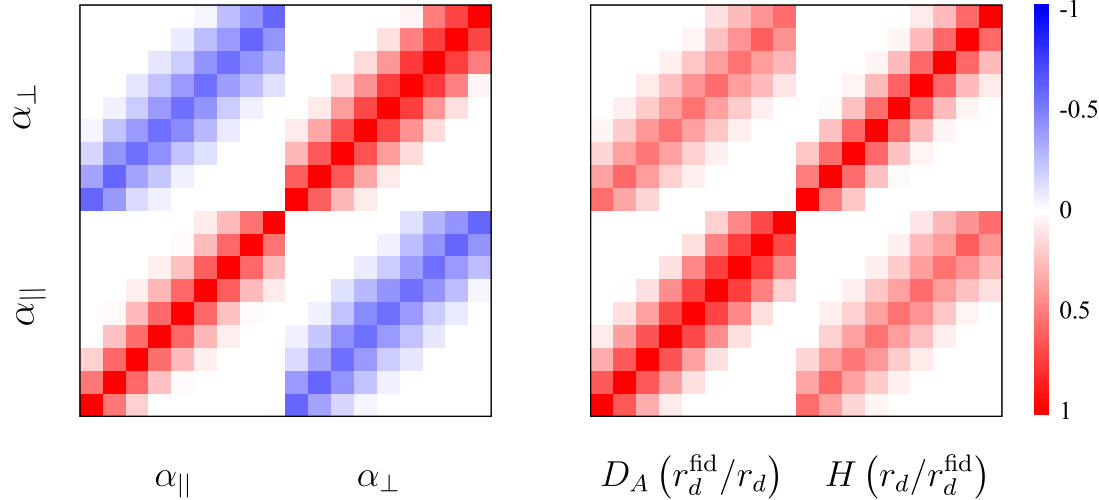


Figure 20. The correlation matrix between α_{\parallel} and α_{\perp} (left) and between $D_A(r_d^{\text{fid}}/r_d)$ and $H(r_d/r_d^{\text{fid}})$ (right) across all the redshift slices.

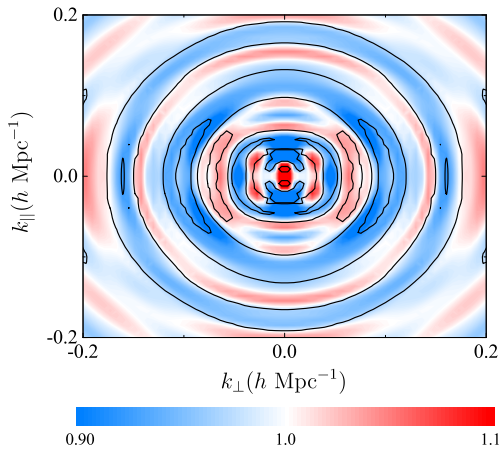


Figure 16. The 68 and 95% CL contour plots for α_{\parallel} and α_{\perp} using $P(k)$ multipoles measured from the DR12 galaxy sample in nine redshift slices. The unfilled black and filled blue contours are results using galaxies in the NGC, and all galaxies in the catalogue respectively. The white cross in each panel illustrates the fiducial model ($\alpha_{\parallel} = \alpha_{\perp} = 1$).

BAO measurements and the three-bin DR12 consensus measurements are consistent well within 68% CL, while tomographic BAO measurements yield a slightly tighter constraint due to the additional tomographic information in redshift, namely,

$$\begin{aligned} w_0 &= -0.96 \pm 0.10; w_a = -0.12 \pm 0.32 \text{ (DR12 Consensus)} \\ w_0 &= -1.01 \pm 0.09; w_a = -0.02 \pm 0.31 \text{ (Tomo. BAO)} \end{aligned} \quad (38)$$

To quantify the improvement on dark energy parameters using tomographic BAO measurement, we also compare to a test case, in which we maximally remove the tomographic information by compressing our nine-bin BAO measurements into a single datapoint at effective redshift $z_{\text{eff}} = 0.475$. We also take out the JLA, WiggleZ and CFHTLenS data from the Base dataset to investigate the strength of the DR12 BAO data more explicitly. The result is shown

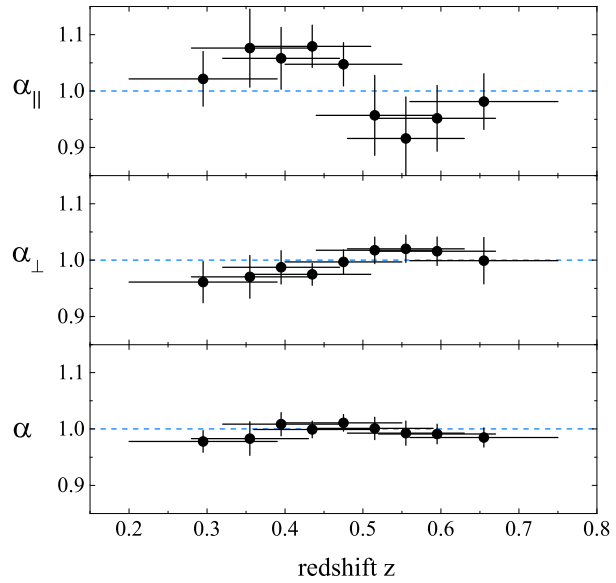


Figure 17. The constraint on the anisotropic BAO dilation parameters α_{\parallel} (top panel), α_{\perp} (middle panel), and the isotropic dilation parameter α (bottom panel). The horizontal and vertical error bars illustrate the width of the redshift bin, and the 68% CL uncertainty, respectively. The horizontal dashed lines show $\alpha_{\parallel} = \alpha_{\perp} = \alpha = 1$ to guide eyes.

in Fig 22,

$$\begin{aligned} w_0 &= -1.20 \pm 0.32; w_a = 0.33 \pm 0.75 \text{ (9 bin)} \\ w_0 &= -1.18 \pm 0.37; w_a = 0.12 \pm 0.89 \text{ (1 bin)} \end{aligned} \quad (39)$$

With tomographic BAO, the 68% CL marginalised errors on w_0 and w_a are reduced by 14% and 16% respectively, and the Figure-

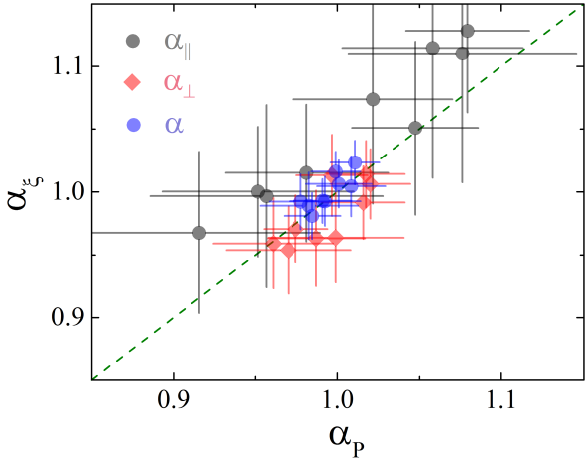


Figure 18. The comparison of our result with that in Wang et al. (2016).

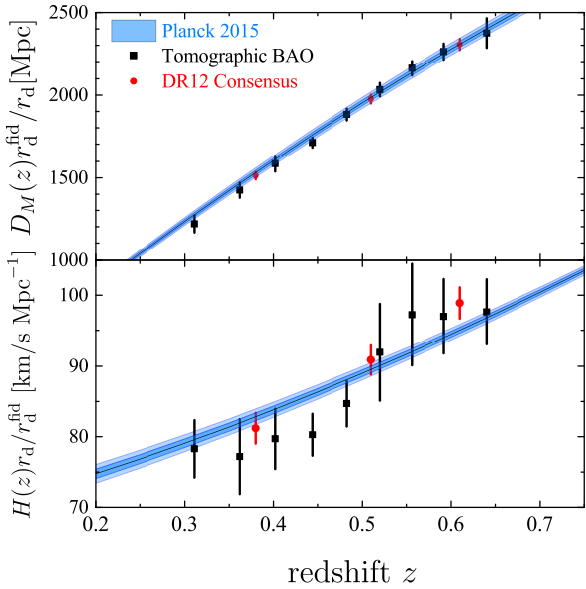


Figure 19. The constraint on D_M and H as a function of redshift, in comparison with the constraints presented in Alam et al. (2016).

of-Merit (FoM), which is the reciprocal of the area of the 68% CL w_0, w_a contour, is improved by 29%.

Tomographic BAO measurements are more informative in terms of the redshift evolution of D_A and H , which are closely related to the time evolution of w . For future galaxy surveys which cover a wider redshift range, the improvement on FoM is expected to be more significant.

6 CONCLUSION

The physics of baryonic acoustic oscillations has been well established to be a robust tool for cosmological studies. Specifically, the BAO measurements make it possible to reconstruct the history of

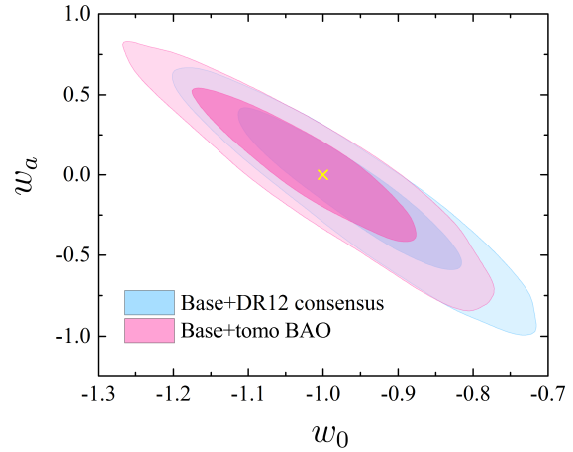


Figure 21. The one-dimensional posterior distribution of w_0, w_a and their two-dimensional 68% and 95% CL contour plots derived from the 9-bin tomographic BAO (blue; filled) and the compressed BAO signal at a single redshift (black; unfilled). The Planck 2015 data are combined to complement.

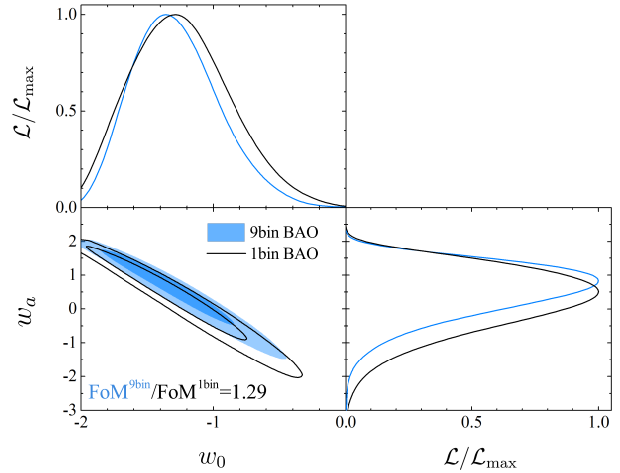


Figure 22. The one-dimensional posterior distribution of w_0, w_a and their two-dimensional 68% and 95% CL contour plots derived from the 9-bin tomographic BAO (blue; filled) and the compressed BAO signal at a single redshift (black; unfilled). The Planck 2015 data are combined to complement.

the cosmic expansion, which is key to reveal the physics of the accelerating expansion of the Universe, and the nature of dark energy.

Obtaining BAO measurements at as many as possible redshifts is ideal for tracing the cosmic expansion history. However, extracting the time evolution of the BAO signal is technically challenging. Naively subdividing the galaxies into multiple independent redshift slices and performing BAO measurements in each slice is a straightforward solution, but the number of slices has to be limited to a small number, otherwise each individual slice would contain too few galaxies to enable a robust BAO measurement due to the low signal-to-noise ratio and issues of systematics.

In this work, we solve this problem using multiple overlapping

redshift slices, which allows for extracting the redshift information of the BAO signal in a large number of redshift slices. We exploit the completed DR12 combined galaxy sample of the BOSS survey, and obtain tomographic BAO measurements in nine overlapping redshift slices using the pre-reconstructed galaxy power spectrum multipoles up to the hexadecapole, after validating our data analysis pipeline using the MD-Patchy mock galaxy catalogues. Our measurement and likelihood routines compatible with CosmoMC are publicly available.

We compare our measurement to that in a companion paper (Wang et al. 2016), which performs similar analysis using galaxy correlation functions derived from the same data sample, and find a consistency. For a further comparison, we derive a three-bin BAO measurement by coherently combining our tomographic measurements, and then compare to the BAO measurement presented in another companion paper (Alam et al. 2016), and find an agreement. The BAO measurements including the full covariance matrices presented in this work and a CosmoMC patch is available at https://sdss3.org/science/boss_publications.php.

We use our BAO measurements to constrain dark energy equation-of-state parameters, and find that for the CPL parametrisation, the Λ CDM model is favoured by a joint dataset of CMB, supernovae, BAO and weak lensing measurement. A more genetic approach for dark energy studies using our measurement will be explored in a separate publication (Zhao et al. 2016).

For the BOSS DR12 sensitivity, we have seen that the dark energy FoM can differ by as much as 29% between cases using tomographic, and non-tomographic BAO measurements. The ongoing and upcoming galaxy redshift surveys, including the eBOSS¹² (Dawson et al. 2015), DESI¹³, Euclid¹⁴ (Amendola et al. 2016), PFS¹⁵ (Takada et al. 2014), and so on, cover a larger and larger cosmic volume, thus there is rich tomographic information in redshifts to be exploited. Besides the method developed in this work, alternatives such as the optimal redshift weighting method (Zhu et al. 2015; Ruggieri et al. 2016; Zhu et al. 2016), are being developed and applied to galaxy surveys.

ACKNOWLEDGEMENTS

GBZ and YW are supported by the Strategic Priority Research Program “The Emergence of Cosmological Structures” of the Chinese Academy of Sciences Grant No. XDB09000000, by National Astronomical Observatories, Chinese Academy of Sciences (NAOC), and by University of Portsmouth. GBZ is supported by the 1000 Young Talents program in China. YW is supported by the NSFC grant No. 11403034. G.R. is supported by the National Research Foundation of Korea (NRF) through NRF-SGER 2014055950 funded by the Korean Ministry of Education, Science and Technology (MoEST), and by the faculty research fund of Sejong University in 2016.

Funding for SDSS-III has been provided by the Alfred P. Sloan Foundation, the Participating Institutions, the National Science Foundation, and the U.S. Department of Energy Office of Science. The SDSS-III web site is <http://www.sdss3.org/>. SDSS-III is managed by the Astrophysical Research Consortium for the Participating Institutions of the SDSS- III Collaboration

¹² <http://www.sdss.org/surveys/eboss/>

¹³ <http://desi.lbl.gov/>

¹⁴ <http://www.euclid-ec.org/>

¹⁵ <http://sumire.ipmu.jp/pfs/>

including the University of Arizona, the Brazilian Participation Group, Brookhaven National Laboratory, Carnegie Mellon University, University of Florida, the French Participation Group, the German Participation Group, Harvard University, the Instituto de Astrofísica de Canarias, the Michigan State/Notre Dame/JINA Participation Group, Johns Hopkins University, Lawrence Berkeley National Laboratory, Max Planck Institute for Astrophysics, Max Planck Institute for Extraterrestrial Physics, New Mexico State University, New York University, Ohio State University, Pennsylvania State University, University of Portsmouth, Princeton University, the Spanish Participation Group, University of Tokyo, University of Utah, Vanderbilt University, University of Virginia, University of Washington, and Yale University.

This research used resources of the National Energy Research Scientific Computing Center, which is supported by the Office of Science of the U.S. Department of Energy under Contract No. DE-AC02-05CH11231, the SCIAMo cluster supported by University of Portsmouth, and the ZEN cluster supported by NAOC.

REFERENCES

- Alam S. et al., 2015, ApJS, 219, 12
 Alam S. et al., 2016, ArXiv e-prints: 1607.03155
 Alcock C., Paczynski B., 1979, Nature, 281, 358
 Amendola L. et al., 2016, ArXiv e-prints: 1606.00180
 Anderson L. et al., 2014a, MNRAS, 441, 24
 Anderson L. et al., 2014b, MNRAS, 441, 24
 Anderson L. et al., 2012, MNRAS, 427, 3435
 Armendariz-Picon C., Mukhanov V., Steinhardt P. J., 2000, Physical Review Letters, 85, 4438
 Asorey J., Crocce M., Gaztañaga E., Lewis A., 2012, MNRAS, 427, 1891
 Ballinger W. E., Peacock J. A., Heavens A. F., 1996, MNRAS, 282, 877
 Betoule M. et al., 2014, A&A, 568, A22
 Beutler F. et al., 2011, MNRAS, 416, 3017
 Beutler F. et al., 2016a, ArXiv e-prints: 1607.03149
 Beutler F. et al., 2016b, ArXiv e-prints: 1607.03150
 Bianchi D., Gil-Marín H., Ruggieri R., Percival W. J., 2015, MNRAS, 453, L11
 Blake C. et al., 2011, MNRAS, 418, 1707
 Bolton A. S. et al., 2012, AJ, 144, 144
 Caldwell R. R., 2002, Physics Letters B, 545, 23
 Chevallier M., Polarski D., 2001, International Journal of Modern Physics D, 10, 213
 Chuang C.-H. et al., 2016, MNRAS, 461, 3781
 Clifton T., Ferreira P. G., Padilla A., Skordis C., 2012, Phys. Rep., 513, 1
 Cole S. et al., 2005, MNRAS, 362, 505
 Cuesta A. J. et al., 2016, MNRAS, 457, 1770
 Dawson K. S. et al., 2015, ArXiv e-prints: 1508.04473
 Eisenstein D. J., Hu W., 1998, ApJ, 496, 605
 Eisenstein D. J., Seo H.-J., Sirko E., Spergel D. N., 2007a, ApJ, 664, 675
 Eisenstein D. J., Seo H.-J., White M., 2007b, ApJ, 664, 660
 Eisenstein D. J., Seo H.-J., White M., 2007c, ApJ, 664, 660
 Eisenstein D. J. et al., 2011, AJ, 142, 72
 Eisenstein D. J. et al., 2005, ApJ, 633, 560
 Fang W., Hu W., Lewis A., 2008, Phys. Rev. D, 78, 087303
 Feldman H. A., Kaiser N., Peacock J. A., 1994, ApJ, 426, 23

- Feng B., Wang X., Zhang X., 2005, Physics Letters B, 607, 35
- Fukugita M., Ichikawa T., Gunn J. E., Doi M., Shimasaku K., Schneider D. P., 1996, AJ, 111, 1748
- Gil-Marín H. et al., 2015, ArXiv e-prints: 1509.06373
- Grieb J. N. et al., 2016, ArXiv e-prints: 1607.03143
- Gunn J. E. et al., 2006, AJ, 131, 2332
- Guo H., Zehavi I., Zheng Z., 2012, ApJ, 756, 127
- Hamilton A. J. S., 2000, MNRAS, 312, 257
- Hartlap J., Simon P., Schneider P., 2007, A&A, 464, 399
- Heymans C. et al., 2013, MNRAS, 432, 2433
- Jing Y. P., 2005, ApJ, 620, 559
- Kaiser N., 1987, MNRAS, 227, 1
- Kitaura F.-S. et al., 2016a, Physical Review Letters, 116, 171301
- Kitaura F.-S. et al., 2016b, MNRAS, 456, 4156
- Leauthaud A. et al., 2016, MNRAS, 457, 4021
- Lewis A., Bridle S., 2002, Phys. Rev. D, 66, 103511
- Lewis A., Challinor A., Lasenby A., 2000, ApJ, 538, 473
- Linder E. V., 2003, Physical Review Letters, 90, 091301
- Padmanabhan N., White M., 2009, Phys. Rev. D, 80, 063508
- Parkinson D. et al., 2012, ArXiv e-prints: 1210.2130
- Peebles P. J. E., Ratra B., 1988, ApJ, 325, L17
- Peebles P. J. E., Yu J. T., 1970, ApJ, 162, 815
- Percival W. J. et al., 2010, MNRAS, 401, 2148
- Percival W. J. et al., 2014, MNRAS, 439, 2531
- Perlmutter S. et al., 1999, ApJ, 517, 565
- Planck Collaboration et al., 2015, ArXiv e-prints: 1502.01582
- Ratra B., Peebles P. J. E., 1988, Phys. Rev. D, 37, 3406
- Reid B. et al., 2016, MNRAS, 455, 1553
- Riess A. G. et al., 1998, AJ, 116, 1009
- Rodríguez-Torres S. A. et al., 2016, MNRAS, 460, 1173
- Ross A. J. et al., 2016, ArXiv e-prints: 1607.03145
- Ross A. J. et al., 2011, MNRAS, 417, 1350
- Ruggeri R., Percival W., Gil-Marín H., Zhu F., Zhao G., Wang Y., 2016, ArXiv e-prints: 1602.05195
- Sahni V., Starobinsky A., 2006, International Journal of Modern Physics D, 15, 2105
- Saito S. et al., 2016, MNRAS, 460, 1457
- Salazar-Albornoz S. et al., 2016, ArXiv e-prints: 1607.03144
- Sanchez A. G. et al., 2016a, ArXiv e-prints: 1607.03146
- Sanchez A. G. et al., 2016b, ArXiv e-prints: 1607.03147
- Scoccimarro R., 2015, Phys. Rev. D, 92, 083532
- Sefusatti E., Crocce M., Scoccimarro R., Couchman H., 2015, ArXiv e-prints: 1512.07295
- Seo H.-J., Beutler F., Ross A. J., Saito S., 2015, ArXiv e-prints: 1511.00663
- Seo H.-J., Eisenstein D. J., 2007, ApJ, 665, 14
- Seo H.-J., Siegel E. R., Eisenstein D. J., White M., 2008, ApJ, 686, 13
- Slepian Z. et al., 2016, ArXiv e-prints: 1607.06097
- Smee S. A. et al., 2013, AJ, 146, 32
- Sunyaev R. A., Zeldovich Y. B., 1970, Ap&SS, 7, 3
- Takada M. et al., 2014, PASJ, 66, R1
- Wang Y. et al., 2016, ArXiv e-prints: 1607.03154
- Weinberg D. H., Mortonson M. J., Eisenstein D. J., Hirata C., Riess A. G., Rozo E., 2013, Phys. Rep., 530, 87
- Wilson M. J., Peacock J. A., Taylor A. N., de la Torre S., 2015, ArXiv e-prints: 1511.07799
- Yamamoto K., Nakamichi M., Kamino A., Bassett B. A., Nishioka H., 2006, PASJ, 58, 93
- Zhao G.-B., Crittenden R. G., Pogosian L., Zhang X., 2012, Physical Review Letters, 109, 171301
- Zhao G.-B., Xia J.-Q., Li M., Feng B., Zhang X., 2005, Phys. Rev. D, 72, 123515
- Zhao G.-B., et al., 2016. In preparation
- Zhu F., Padmanabhan N., White M., 2015, MNRAS, 451, 236
- Zhu F., Padmanabhan N., White M., Ross A. J., Zhao G., 2016, ArXiv e-prints: 1604.01050